Wellbore stability in high-temperature granite under true triaxial stress

Ryota Goto[a], Kiyotoshi Sakaguchi[a], Francesco Parisio[b], Keita Yoshioka[c], Eko Pramudyo[a], Noriaki Watanabe[a,*]

[a] Department of Environmental Studies for Advanced Society, Graduate School of Environmental Studies, Tohoku University, Sendai 9808579, Japan

[b] Chair of Soil Mechanics and Foundation Engineering, Technische Universitaet Bergakademie Freiberg, Freiberg 09599, Germany

[c] Department of Environmental Informatics, Helmholtz Centre for Environmental Research–UFZ, Leipzig 04318, Germany

*Corresponding author. E-mail address: noriaki.watanabe.e6@tohoku.ac.jp, Tel & Fax: +81-22-795-7384

Abbreviations: AE, acoustic emissions

Abstract

Supercritical/superhot geothermal success depends on successful drilling. However, wellbore stability in supercritical environments has not been investigated because imposing sufficient stress on high-temperature granite with true triaxial loading is difficult. We conducted wellbore failure experiments on 200–450 °C granite under true triaxial stress, including deformation and acoustic emission measurements, and post-experiment thin section observations. Wellbore failure initiated at stress states consistent with existing brittle failure criterion at the studied temperatures. Using breakout geometry for *in situ* stress estimation may be difficult as shear failure propagation is suppressed at high temperatures; however, boreholes may be inherently stable in high-temperature environments.

Keywords: wellbore failure, granite, high temperature, supercritical geothermal environment, superhot geothermal environment, true triaxial stress

1. Introduction

Recent attention in geothermal power generation has focused on methods for harvest geothermal energy from unconventional supercritical (or superhot) geothermal environments that exceed the critical temperature of water (374 °C for pure water and 406 °C for seawater) at drillable depths of approximately 2–4 km, as found in Iceland (Friðleifsson et al., 2014; Friðleifsson and Elders, 2017; Steingrimsson et al., 1990), Italy (Baron and Ungemach, 1981; Batini et al., 1983; Ruggieri and Gianelli, 1995), Japan (Kato et al., 1998), Mexico (Espinosa-Paredes and Garcia-Gutierrez, 2003), and the United States (Fournier, 1991; Garcia et al., 2016). Supercritical geothermal environments can provide superheated steam or supercritical water with an extremely high specific enthalpy exceeding 2 MJ/kg (Elders et al., 2014; Friðleifsson and Elders, 2005; Friðleifsson et al. 2007; Smith and Shaw, 1975, 1979; Tester et al., 2006). Therefore, harvesting supercritical geothermal energy is expected to increase the productivity and sustainability of geothermal energy generation. However, in supercritical geothermal environments on the continental crust, the formation of permeable fracture networks (Tsuchiya et al., 2016; Watanabe et al., 2017a; Weis et al., 2012) can potentially be suppressed by the increased efficiency of mineral crystal plasticity (Parisio et al., 2019, 2020; Tullis and Yund, 1977; Violay et al., 2017), the retrograde solubility of silica minerals (Fournier, 1991; Saishu et al., 2014; Tsuchiya and Hirano, 2007; Watanabe et al., 2021), and the enhanced rates of fracture healing/sealing caused by water–rock reactions (Moore et al., 1994; Morrow et al., 2001; Watanabe et al., 2020). Therefore, it is necessary to develop enhanced geothermal system technologies to artificially create or recreate permeable fracture networks in these supercritical geothermal environments.

Recent studies have suggested that the injection of water at or near its critical temperature into granite is likely to create a dense network of microfractures suitable for geothermal energy extraction, a so-called cloud-fracture network, through continuous infiltration and the stimulation of pre-existing microfractures by the low-viscosity water (Goto et al. 2021; Watanabe et al., 2017b, 2019). Additionally, it has been suggested that the pore pressure required to initiate this flow-induced microfracturing may be well predicted by the Griffith failure criterion, which assumes the initiation of brittle failure from pre-existing fractures and is a function of the maximum and minimum principal stresses and tensile strength of rocks (Cox, 2010; Griffith, 1924; Jaeger and Cook, 1979; Secor, 1965). However, the characteristics of wellbore failure (Ewy and Cook, 1990; Morita and Nagano, 2016), and the possibility of utilizing these failures (i.e., induced fractures and breakout) for in situ stress estimation (Brudy and Zoback, 1999; Kato et al., 1998; Zoback et al., 1985) to achieve safe and effective fracturing at the minimum required injection pressure, remain unclear for supercritical geothermal environments. This is because wellbore failure experiments under true triaxial stress (Lee and Haimson, 1993; Song and Haimson, 1997) have never been conducted on high-temperature granite. To the best of our knowledge, wellbore failure experiments under hydrostatic stress have only been conducted on granite at temperatures up to 600 °C (Zhao et al., 2015).

The aim of this study is to experimentally simulate wellbore failure in granite under true triaxial stress in supercritical geothermal conditions. We first introduce a novel experimental method for assessing high-temperature wellbore failure in relatively large (10-cm cubic) rock samples under true triaxial stress. Subsequently, we present the results of experiments conducted on granite at 200–450 °C, which show non-catastrophic wellbore failure. Finally, we suggest the predictability of the initiation of wellbore failure using an existing failure criterion for rocks and discuss the possibility of estimating in situ stress from wellbore failure.

2. Experimental methods

2.1. Granite and experimental system

Cubes (100 × 100 × 100 mm) of Inada granite from Ibaraki prefecture, Japan (Figure 1), with a single wellbore (diameter: 10 mm, length: 100 mm) at the center, were prepared for the high-temperature wellbore failure experiment under true triaxial stress. Inada granite, of which the porosity at room temperature and atmospheric pressure is 0.5-0.8%, has been used in previous studies on supercritical hydraulic fracturing (Goto et al., 2021; Watanabe et al., 2017b, 2019).

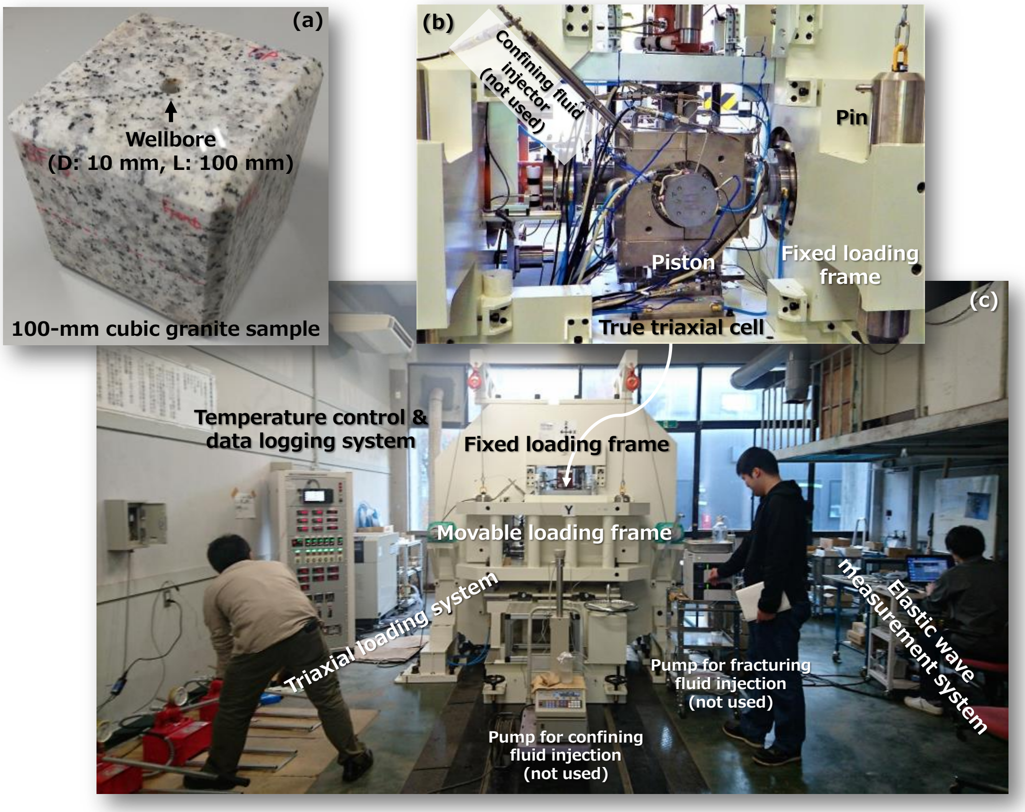

Figure 1. Granite sample (a), high-temperature true triaxial cell (b), and experimental system (c) in the wellbore failure experiment, adapted from Watanabe et al. (2019).

We used the experimental system (Figure 1) originally developed for supercritical hydraulic fracturing by Watanabe et al. (2019) and applied in Goto et al. (2021). The system consisted of a true triaxial cell, a triaxial loading system, a pump for injecting fracturing fluid into the sample, a pump for injecting confining fluid (high-viscosity plastic melt in this system) along the sample edges via an injector, an elastic wave measurement system, and a temperature control and data logging system. In the present experiment, the elastic wave measurement system was an acoustic emission (AE) measurement device (Physical Acoustics Cooperation's two-channel data acquisition and digital signal processing AE system, PCI-2), and the pumps and injector were not used because no fracturing or confining fluids were required for the experiment.

The true triaxial cell (Figure 2) consisted of a pressure vessel with a cubic skeleton, six pistons to apply a compressive load to the 100 × 100 × 100 mm cubic rock sample via a stainless-steel plate (for better mechanical coupling between the piston loading faces and the sample), and thermal insulators used in conjunction with heaters for the pressure vessel. The pressure vessel had six cylindrical holes to allow the pistons to be inserted into the vessel, with graphite packing lubricating the sliding portions. The edges of the sample were chamfered so that the loading face of the sample had 90 mm sides that corresponded to the shape (i.e., 90 × 90 mm) of both the loading face of the piston and the stainless-steel plate. Each piston was equipped with four cartridge heaters and a pipe through which a thermocouple could reach the vicinity of the sample surface, and had an elastic wave guide bar on the opposite side of the loading face. An AE sensor (R15α, 150-kHz resonant frequency sensor, Physical Acoustics Corporation) was attached to the face of the elastic wave guide bar, while two AE sensors were used for one pair of the opposed horizontal pistons, where these pitons were used to apply the far-field maximum horizontal stress described in section (2.2). The temperature of the bar was maintained near ambient conditions using a cooling jacket through which water from a chiller circulated.

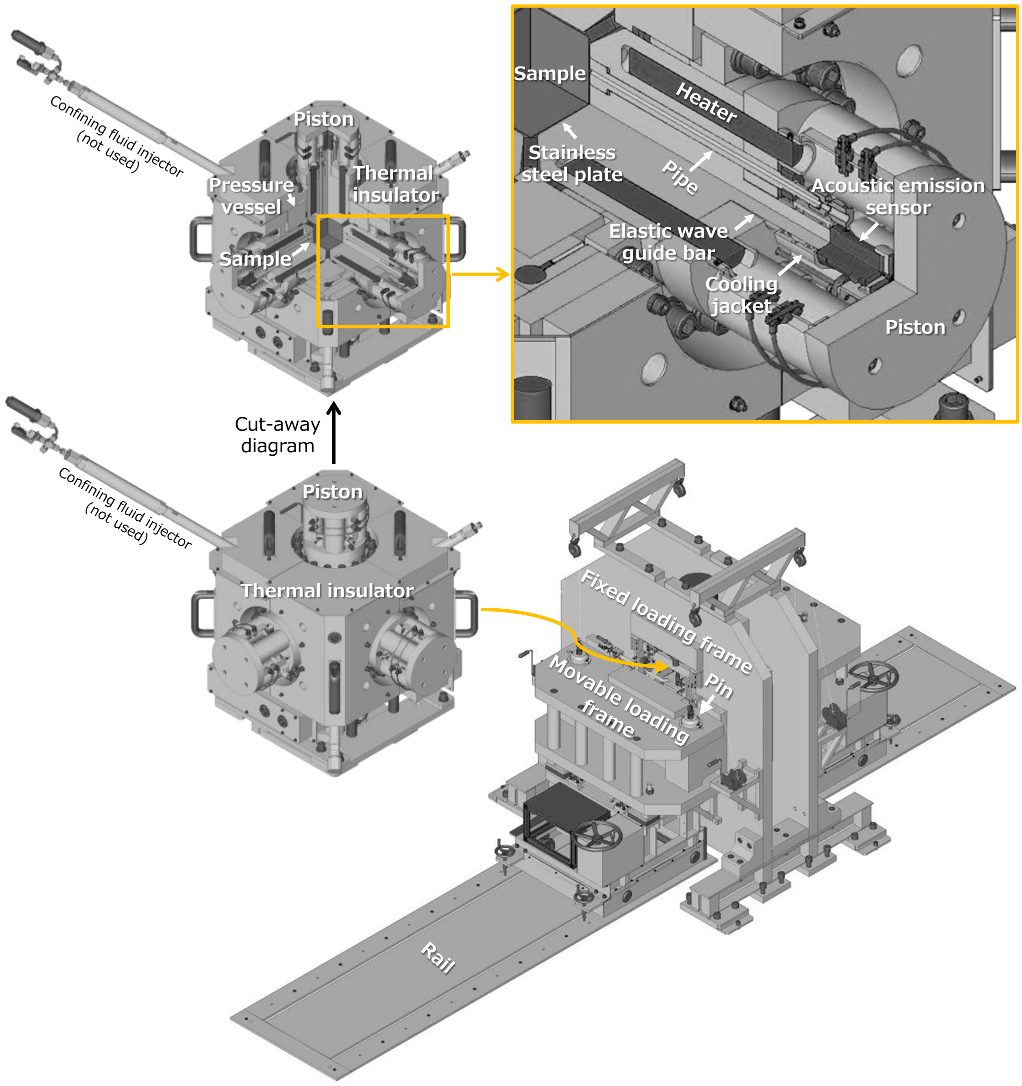

Figure 2. Three-dimensional design of the high-temperature true triaxial cell and triaxial loading frame, adapted from Watanabe et al. (2019).

The triaxial loading system (Figure 2) comprised a fixed loading frame and a movable loading frame. The fixed frame had two hydraulic rams that were placed vertically and horizontally. The movable loading frame contained a horizontal hydraulic ram. Each hydraulic ram had a capacity of 3 MN and was actuated using a manual oil pump. The true triaxial cell was placed on the loading platform of the fixed frame extremely carefully to prevent any loading eccentricity. It was then connected to the AE measurement system and the temperature control and data logging system. When a compressive load was applied, the movable loading frame engaged with the fixed loading frame via four cylindrical pins.

The triaxial loading system independently applied compressive loads in three orthogonal directions, using a single hydraulic ram with a fixed loading platen on the opposite side. The hydraulic ram, equipped with a load cell, pushed the piston of the true triaxial cell via a spherical seated platen. The displacement of the piston was ascertained as a proxy for sample deformation, using a linear variable differential transformer displacement transducer. The displacement transducer was attached to a cantilever attached to the fixed loading platen side, so that the measured displacement excluded any expansion between opposing platens caused by loading frame deformation in response to large loads.

2.2. Experimental procedures and conditions

The first procedure involved increasing the temperature of the pressure vessel and pistons to a prescribed value (200, 350, or 450 °C) while a hydrostatic load (approximately 1 MPa) was applied to a sample with a vertical wellbore. Once the temperature reached the prescribed value, the sample was subjected to an initial stress state with a hydrostatic pressure of 53 MPa. To induce wellbore failure, one of the horizontal stresses, referred to as the far-field minimum horizontal stress (σ_h) in this study, was then decreased continuously and gradually to approximately 5 MPa by returning oil to the manual oil pump, while the far-field maximum horizontal stress (σ_H) and the vertical stress (σ_V) remained constant at the initial level. The manual oil pump was equipped with a flow control valve so that the load could be continuously decreased by returning oil to the pump using a constant valve opening.

For post-mortem analysis, the sample was impregnated with a thermosetting acrylic resin under vacuum conditions and then heated to 50 °C under atmospheric pressure, so that the cured resin preserved structural changes within the sample. The resin-impregnated sample was cut horizontally across the middle region containing the wellbore, and a thin section of the inner region was prepared to assess wellbore failure via optical microscopy.

Based on Kirsch's equations (Gholami et al., 2014; Hiramatsu and Oka, 1968; Kirsch, 1898), the state of stress around the wellbore in isotopic elastic homogenous rocks in a cylindrical coordinate system (r, θ, z), for which r (from the center of the wellbore), θ (from the σ_H direction), and z correspond to the radial, tangential, and axial (vertical) directions of the wellbore, respectively, may be estimated as follows:

$$\sigma_r = \frac{1}{2}(\sigma_H + \sigma_h)\left(1 - \frac{R^2}{r^2}\right) + \frac{1}{2}(\sigma_H - \sigma_h)\left(1 - \frac{4R^2}{r^2} + \frac{3R^4}{r^4}\right)\cos(2\theta) + P_w\frac{R^2}{r^2}, \qquad (1)$$

$$\sigma_\theta = \frac{1}{2}(\sigma_H + \sigma_h)(1 + \frac{R^2}{r^2}) - \frac{1}{2}(\sigma_H - \sigma_h)(1 + \frac{3R^4}{r^4})\cos(2\theta) - P_w\frac{R^2}{r^2}, \text{ and} \qquad (2)$$

$$\sigma_z = \sigma_V - 2\nu(\sigma_H - \sigma_h)\cos(2\theta), \qquad (3)$$

where σ_r, σ_θ, and σ_z are the radial, tangential, and axial stresses, respectively, R is the radius of the wellbore, Pw is the internal wellbore pressure, and ν is the Poisson's ratio, where P_w is assumed to be zero for the experiments under dry condition in this study. Notably, the applicability of Kirsch's equations on a wellbore in the granite used in the present study has been previously confirmed via a hydraulic fracturing experiment on the same granite (diameter: 30 mm, length: 25 mm) with a wellbore (diameter: 1.5 mm, length: 10 mm) (Watanabe et al., 2017b).

Based on the Hoek–Brown failure criterion, a well-known empirical wellbore failure surface (Hoek and Brown, 1980; Pariseau, 2009) is represented by

$$(\sigma_1 - \sigma_3)^2 - (A\sigma_3 + B^2) = 0, \qquad (4)$$

$$A = \frac{\sigma_c^2 - \sigma_t^2}{\sigma_t}, \text{ and} \qquad (5)$$

$$B = \sigma_c, \qquad (6)$$

where σ_1, σ_2, and σ_3 are the maximum, intermediate, and minimum principal stresses, respectively, and σ_c and σ_t are the unconfined compressive and tensile strengths, respectively.

According to the literature, the σ_c of the granite used in this study is approximately 150 MPa at 200 °C, 130 MPa at 350 °C, and 120 MPa at 450 °C (Sakai, 1987), while the σ_t and ν of the same granite remain relatively constant across the range of experimental temperatures, approximately 6 MPa and 0.2, respectively (Kinoshita et al., 1997). Using these values, the Hoek–Brown failure criterion provides the following predictions regarding the initiation of tensile and shear failures at $\theta = 0°$ and 90° for the wellbore (Figure 3). Tensile failure, which may produce tensile fractures, by increasing the σ_θ under tension at $\theta = 0°$ starts at the same σ_h level at all temperatures because σ_t is temperature-independent. In contrast, shear failure, which may cause breakout, by increasing the σ_θ under compression at $\theta = 90°$ is initiated at higher σ_h values (i.e., smaller σ_θ) at higher temperatures, because of the smaller σ_c. Table 1 lists these estimated and predicted values. According to our computations, we expect non-catastrophic failure producing millimeter-scale breakout and/or tensile fractures, because the significantly increased σ_θ in both the compression and tension is contained to within 10 mm of the wellbore under the final state of far-field stress (Eq. 2).

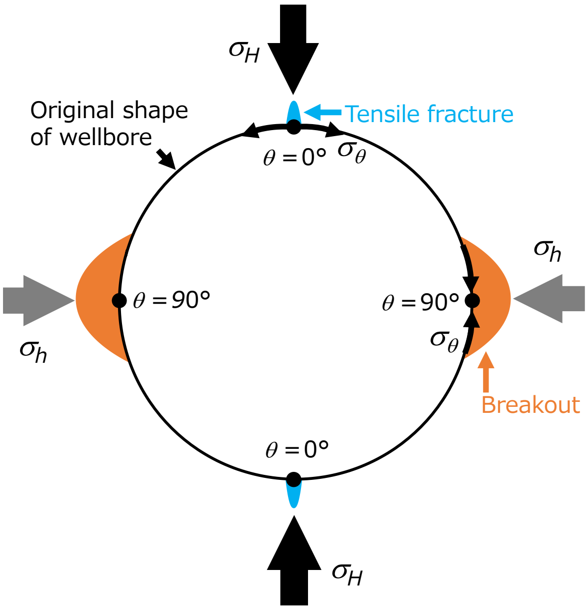

Figure 3. Conceptual illustration of breakout and tensile fractures in the wellbore wall, caused by shear and tensile failures, respectively.

Table 1. Estimated unconfined compressive and tensile strengths (σ_c and σ_t) and predicted far-field minimum horizontal stress (σ_h) for shear and tensile failures at each experimental temperature.

Temperature (°C)	σ_c (MPa)	σ_t (MPa)	σ_h at failure (MPa)	
			Shear failure	Tensile failure
200	150	6	6	15
350	130	6	26	15
450	120	6	36	15

3. Results and discussion

3.1. Temporal changes in stress, resultant behaviors of displacement and AE

Figures 4–6 show temporal changes in the far-field stresses (σ_h, σ_H, and σ_V) and corresponding changes in the estimated stresses on the wellbore (σ_θ and σ_z) using Eqs. 2 and 3, the displacement of the piston (a proxy of sample deformation) in the σ_H and σ_V directions, and the AE energy with its cumulative value, for the three experiments at 200, 350, and 450 °C. In the AE measurement device used in this study, AE energy is calculated as the time integral of the absolute signal voltage and reported in arbitrary units (a.u.). AE energy shown herein is the sum of the values obtained from the two AE sensors; we conducted the experiment at 450 °C, twice, and confirmed the absence of significant large AE energy in the second experiment (i.e., after failure in the first experiment) as illustrated in Supplementary Figure S1.

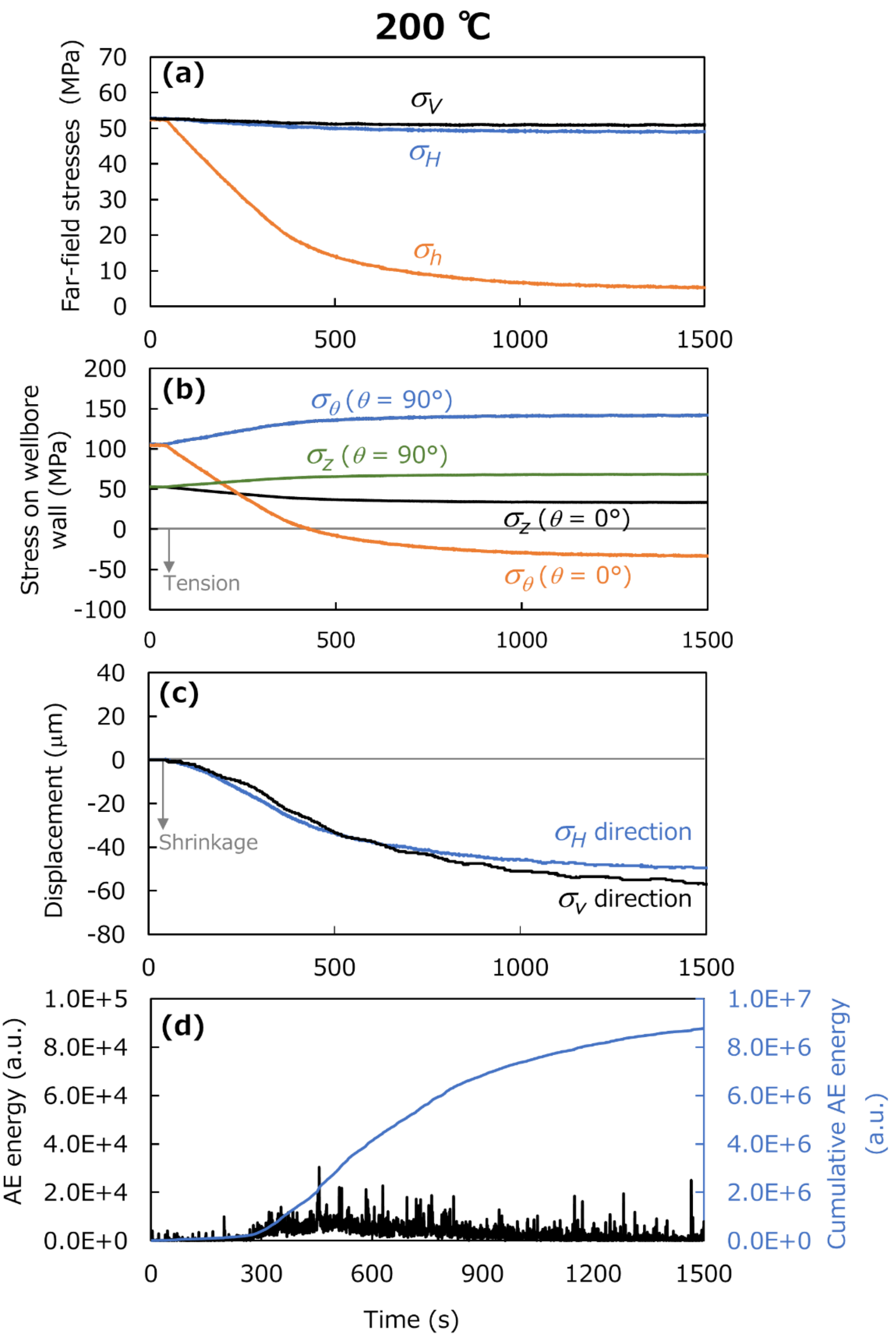

Figure 4. Temporal changes in the far-field stresses (a) and corresponding changes in the estimated stresses on the wellbore wall (b), displacement of the piston (c), and acoustic emission (AE) energy and its cumulative value (d), in the experiment at 200 °C.

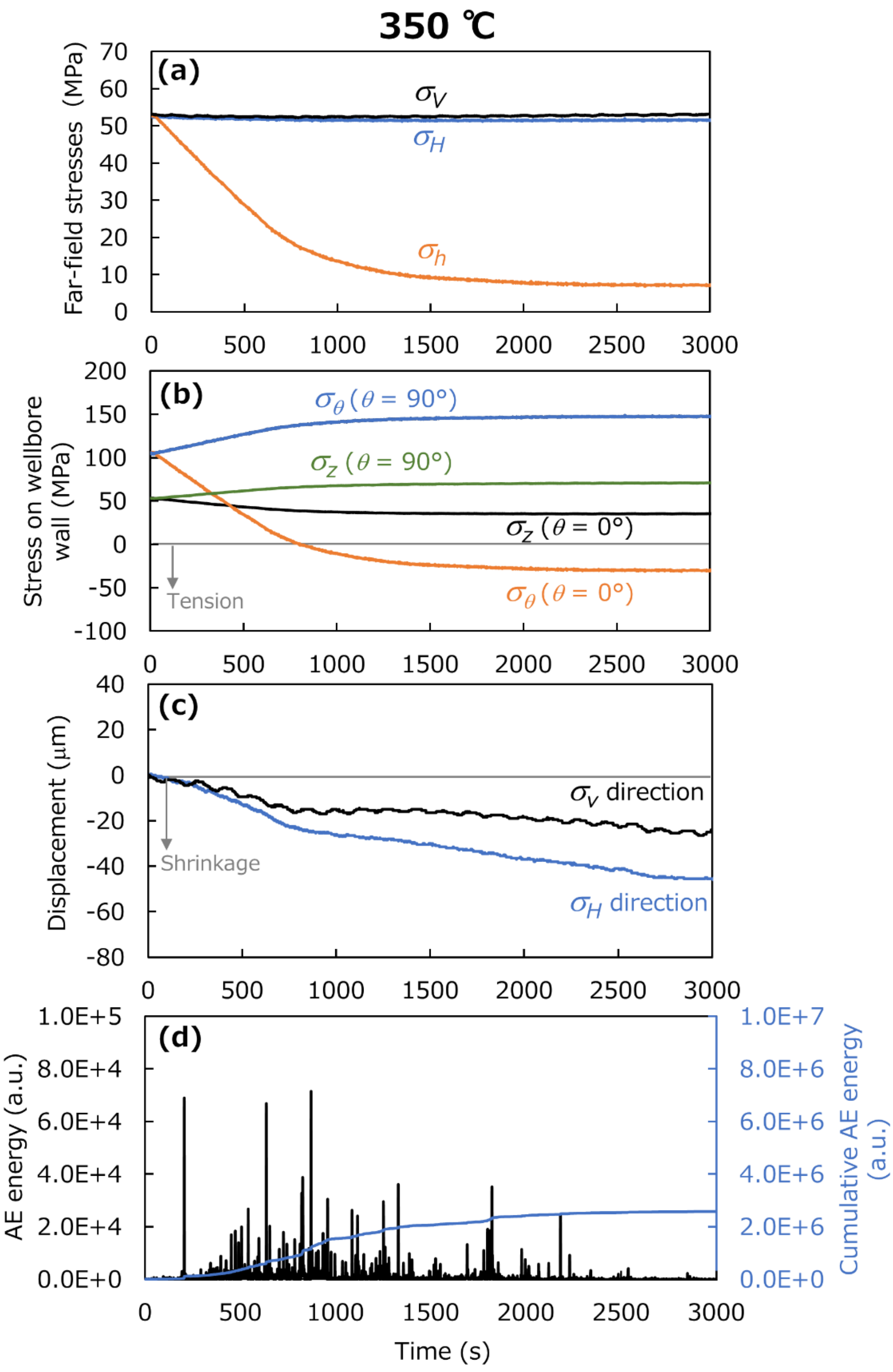

Figure 5. Temporal changes in the far-field stresses (a) and corresponding changes in the estimated stresses on the wellbore wall (b), displacement of the piston (c), and acoustic emission (AE) energy and its cumulative value (d), in the experiment at 350 °C.

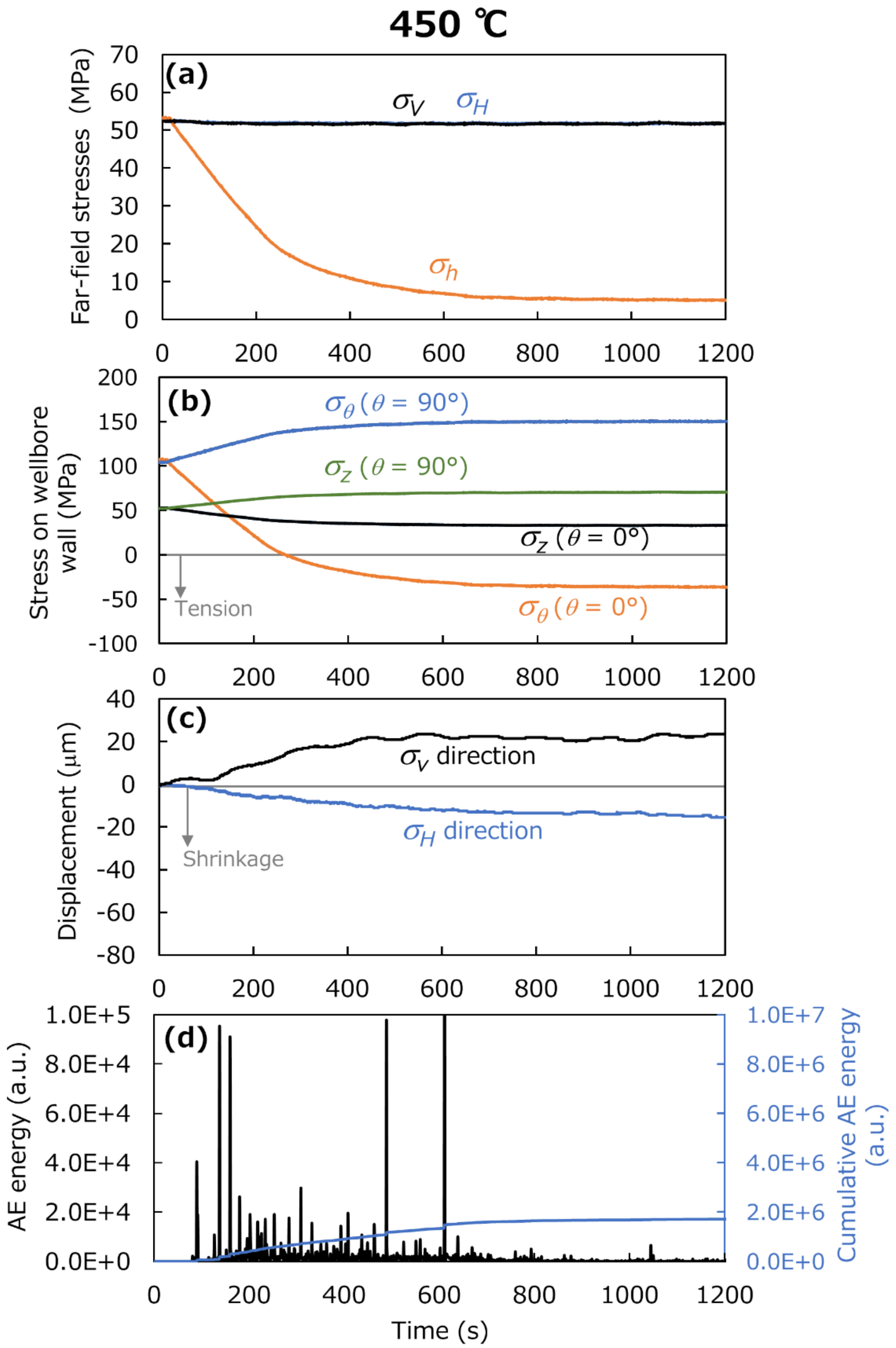

Figure 6. Temporal changes in the far-field stresses (a) and corresponding changes in the estimated stresses on the wellbore wall (b), displacement of the piston (c), and acoustic emission (AE) energy and its cumulative value (d), in the experiment at 450 °C.

In all the experiments, we were able to decrease σ_h smoothly up to approximately 5 MPa by transferring the oil back to the manual oil pump, while σ_V and σ_H remained almost constant. The rate of σ_h change was faster for higher σ_h (oil pressure) because the flow control valve opening was kept constant (Figures 4a, 5a, and 6a). The rate of σ_h decline in the experiment at 350 °C was slower than those in the other two experiments because it was conducted at a lower room temperature in winter, which affected the oil viscosity. The final σ_h level in each experiment exceeded the predicted criteria for shear failure (6–36 MPa at 450–200 °C) and/or tensile failure (15 MPa at all temperatures) of the wellbore (Table 1). σ_θ and σ_z also changed nonlinearly in response to nonlinear changes in σ_h (Figures 4b, 5b, and 6b). At $\theta = 0°$ (θ as defined in Figure 3), σ_θ decreased to −30 to −40 MPa (i.e., 30–40 MPa in tension), whereas at $\theta = 90°$, σ_θ increased to approximately 140–150 MPa.

Although the final σ_h in each experiment exceeded the predicted criteria for the shear failure and/or tensile failure of the wellbore, the changes in displacement (Figures 4c, 5c, and 6c) and cumulative AE energy (Figures 4d, 5d, and 6d) in all experiments were continuous before reaching a plateau, suggesting non-catastrophic shear and tensile failures, as illustrated in Figure 3. The displacement data at 200 °C indicate that the sample shrank similarly in both the σ_H and σ_V directions with decreasing σ_h. With increasing temperature, the sample shrank less in the σ_V and/or σ_H directions, and it dilated in the σ_V direction at 450 °C. Additionally, we observed that the AE energy behavior changed with increasing temperature. For low temperatures, we recorded smaller AE energies frequently. In contrast, at high temperatures, higher AE energies were recorded infrequently, resulting in a lower cumulative AE energy. These changes in displacement and AE behavior with increasing temperature may have been caused by the predicted shift in the predominant failure mode of the wellbore from tensile to shear failure (Table 1).

3.2. Wellbore failure prediction

Figures 7–9 show the changes in the displacement of the piston and AE energy as a function of σ_h in each experiment, together with the predicted σ_h for the shear and tensile failure of the wellbore. Although the sample shrank continuously in both the σ_H and σ_V directions throughout the experiment at 200 °C, the shrinkage accelerated when the loading reached the predicted tensile failure threshold (the stress path is indicated by the green arrow in Figure 7a). Additionally, we recorded large AE energy events, as indicated by the blue arrow, when σ_h reached the predicted tensile failure threshold (Figure 7b). This suggests that the tensile failure of the wellbore started around the expected σ_h level and tensile fractures were generated in the σ_V–σ_H plane, as illustrated in Figure 3, meaning that the sample deformed more easily in the σ_V and σ_H directions. We recorded another set of large AE energy events, as indicated by the red arrow, around the predicted shear failure threshold. However, after the presumed tensile failure, the stress field was altered and the initial shear failure prediction may no longer have been valid. Indeed, the displacement behavior did not change, despite the second set of large AE energy events.

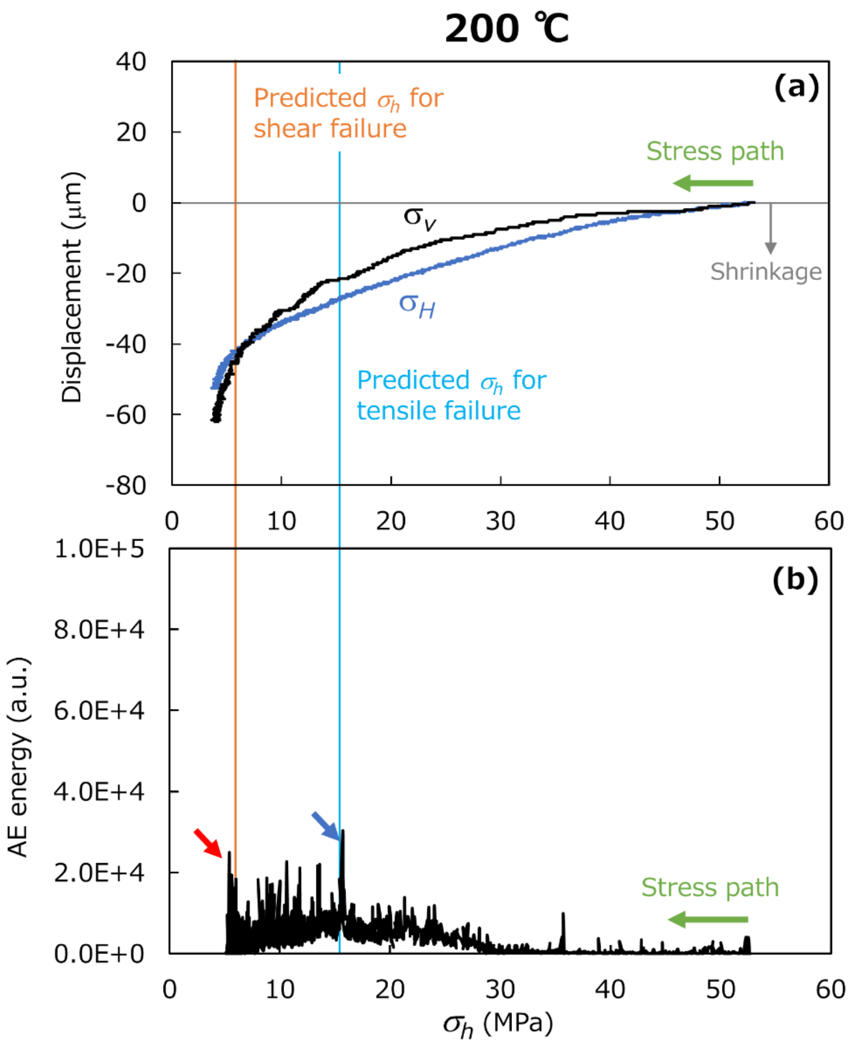

Figure 7. Changes in the displacement of the piston (a) and acoustic emission (AE) energy (b) as a function of σ_h in the experiment at 200 °C, together with the predicted σ_h for the shear and tensile failure of the wellbore wall.

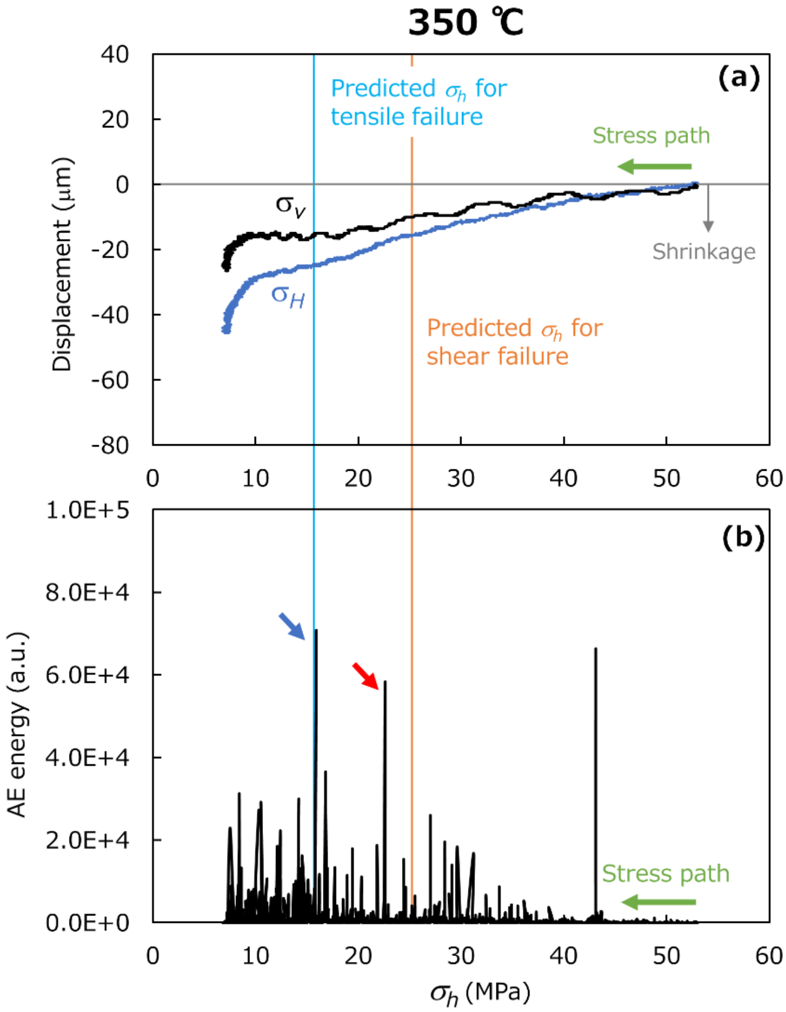

Figure 8. Changes in the displacement of the piston (a) and acoustic emission (AE) energy (b) as a function of σ_h in the experiment at 350 °C, together with the predicted σ_h for the shear and tensile failure of the wellbore wall.

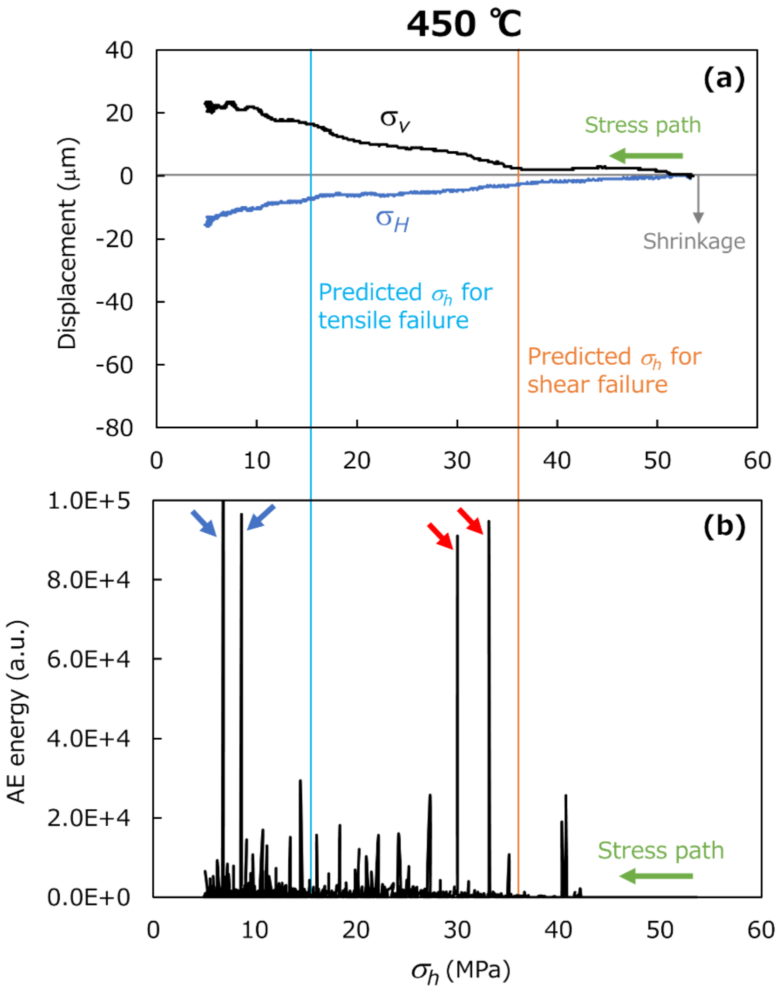

Figure 9. Changes in the displacement of the piston (a) and acoustic emission (AE) energy (b) as a function of σ_h in the experiment at 450 °C, together with the predicted σ_h for the shear and tensile failure of the wellbore wall.

In contrast, at 450 °C, significant dilation in the σ_V direction started after the predicted shear failure loading (Figure 9a) and large energy AE events occurred, as indicated by the red arrows in Figure 9b. This suggests the occurrence of wellbore shear failure that caused dilation in the σ_V direction, as Zhao et al. (2015) observed shear failure and increased axial deformation in a wellbore in granite under hydrostatic stress. After the predicted tensile failure, remarkably large energy AE events occurred again, as indicated by the blue arrows in Figure 9b. However, the second set of large energy AE events occurred at a much smaller σ_h than the predicted value for tensile failure, and there was no clear indication of tensile failure in the deformation behavior. This suggests that shear failure dominated the wellbore failure throughout the experiment at 450 °C.

In the 350 °C experiment (Figure 8), after the sample reached the predicted shear failure, the σ_h-dependence of the shrinkage in the σ_V direction decreased, flattening the displacement curve at an σ_h of approximately 10–20 MPa. Based on the discussion of the 450 °C experiment, this change in displacement behavior can be attributed to shear failure inducing dilation in the σ_V direction. Subsequently, at σ_h < 10 MPa, the σ_h-dependence of the shrinkage in both the σ_V and σ_H directions increased. Based on the discussion of the 200 °C experiment, this can be attributed to tensile failure inducing shrinkage in both the σ_V and σ_H directions. Indeed, we recorded large AE energies, as indicated by the red and blue arrows, around the predicted shear and tensile failures. This suggests that, at 350 °C, both shear and tensile failure significantly contributed to wellbore failure, owing to their relatively similar σ_h levels.

The above discussion suggests that the wellbore failure in the present experiments occurred at σ_h levels that were largely consistent with the predicted values (Table 1). Therefore, it is possible to predict wellbore failure in supercritical geothermal environments based on existing rock failure criterion, such as the Hoek–Brown criterion used in this study.

3.3. Possibility of using wellbore failure for in situ stress estimation

Figure 10 shows optical microphotographs of the thin sections prepared from the samples after the experiment (Figure 10a–c) and from an intact sample, for comparison, which was not used in any experiment (Figure 10d). In these microphotographs, the profile of the wellbore is traced in red, whereas the yellow line indicates a perfect circle

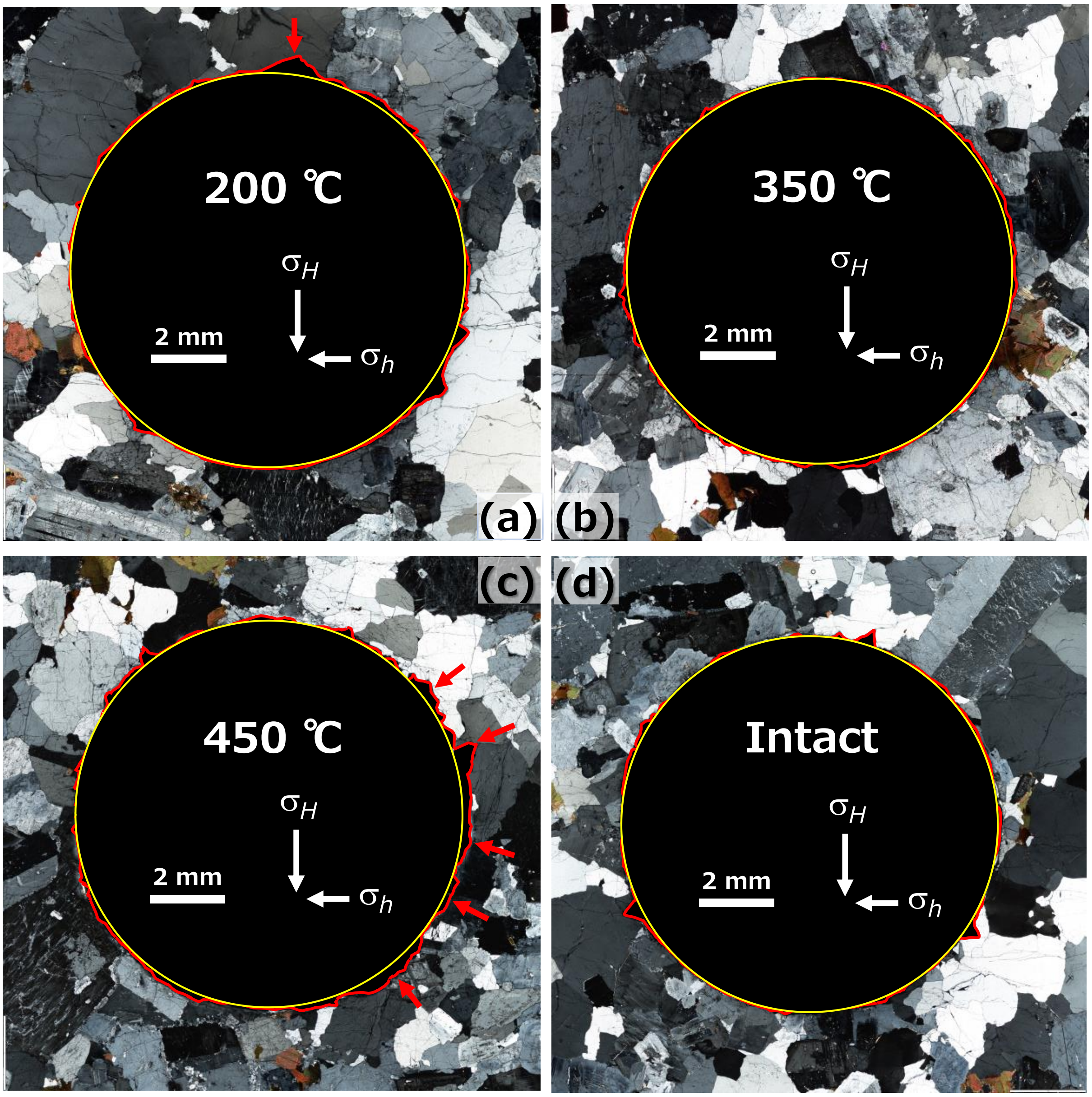

Figure 10. Optical microphotographs of thin sections prepared from the samples after the experiments at 200 (a), 350 (b), and 450 °C (c), and from an intact sample for comparison (d).

Even the intact sample profile does not completely match the perfect circle because of the relatively small defects with acute triangular shapes caused by boring (Figure 10d). However, the 200 °C profile deviates more from the perfect circle owing to the presence of larger defects in the wellbore, as indicated by the red arrow in Figure 10a. The largest defect appears to be a tensile fracture produced by the dominant failure at 200 °C (i.e., tensile failure at $\theta = 0°$ in Figure 3). The 450 °C profile also deviated significantly from the perfect circle owing to the presence of much broader defects, as indicated by the red arrows (Figure 10c). The defects appear to be breakouts produced by the dominant failure at 450 °C (i.e., shear failure at $\theta = 90°$ in Figure 3). The changes in the wellbore shape are consistent with our speculation that the dominant failure mode shifts from tensile (200 °C) to shear (450 °C). In contrast, the 350 °C profile did not significantly deviate from the perfect circle, although small deviations appear around the entire wellbore wall (Figure 10b). It would therefore be reasonable to assume no clear defects at specific locations if, as suggested in the previous section (3.2), both shear and tensile failure significantly contributed to the wellbore failure at 350 °C.

The present experimental results therefore suggest that breakout and tensile fractures may occur in wellbores in supercritical geothermal environments. However, at either 350 °C or 450 °C, we did not observe the textbook breakout shape (Figure 3), such as the shape observed in previous studies on granite at room temperature (Lee and Haimson, 1993; Song and Haimson, 1997). This suggests that high temperatures suppress the propagation of shear failure and its formation of clear breakout patterns. This may have been related to the intermittent large energy AE events at 350 and 450 °C (Figures 5d and 6d), because such intermittent large AE events were not observed in the previous study (Lee and Haimson, 1993). This, in turn, suggests that in situ stress estimation from the shape of the breakout would be difficult in supercritical geothermal environments because of the suppression of failure propagation at high temperatures. However, if shear failure propagation is suppressed and wellbore failure does not propagate further into the formation at high temperatures, this would greatly improve wellbore stability and suggests the possibility of underbalanced drilling, which would substantially reduce the risk of circulation loss during drilling. If our conclusions are correct, they would have tremendous implications for drilling practices in supercritical geothermal development. The suppressed failure propagation from the wellbore wall into the rock may have been caused by a rapid relaxation of stress concentration around the wellbore since several points on the circumference of the wellbore wall simultaneously reached failure, or became close, due to the relatively small unconfined compressive strength. However, this was not confirmed, hence warrants further investigation. Thus, extensive future studies are encouraged to examine the suppression of failure propagation at high temperatures and to clarify the mechanisms involved. Ideally, such studies should address wellbore failure in high-temperature granite along the temperature and stress paths that may occur during drilling, with considerations on influences of fluid pressure and thermal stress as well as *in situ* preexisting weakness planes.

4. Conclusions

For the successful development of enhanced geothermal systems in supercritical geothermal environments through hydraulic fracturing, it is essential to establish wellbore stability and understand in situ stresses. The results of the first experiments on wellbore failure in 200–450 °C granite under true triaxial stress suggest that non-catastrophic tensile and shear failure occurs in the wellbore at such temperatures, and their initiation is predictable based on existing brittle failure criterion for rocks. The results also suggest that the resultant shape of the wellbore after failure, particularly after breakout by shear failure, is not ideal for in situ stress estimation, because of the suppressed propagation of shear failure at high temperatures. In other words, there is a possibility that the high temperatures in supercritical geothermal environments contribute to wellbore stability. Therefore, extensive future studies are encouraged to examine the suppression of failure propagation at high temperatures and to clarify the underlying mechanisms.

Acknowledgments

This study was supported in part by the Japan Society for the Promotion of Science (JSPS) through Grants-in-Aid for Scientific Research (B) [Grant Number 17H03504], Challenging Research (Pioneering) [Grant Number 21K18200], and JSPS Fellows [Grant Number 20J2020108]. This study was also supported by JSPS and the Deutsche Forschungsgemeinschaft (DFG, German Research Foundation) under the Joint Research Program (JRPs-LEAD with DFG) [Grant Number JPJSJRP20181605]. K.Y. was funded by the German Federal Ministry of Education and Research (BMBF) for the GeomInt project [Grant Number 03G0866A], within the BMBF Geoscientific Research Program "Geo:N Geosciences for Sustainability." F.P. was funded by DFG, Project number PA 3451/1-1. The authors would also like to thank Toei Scientific Industrial Co., Ltd., for manufacturing the experimental system.

Data availability

The data supporting the findings of this study are available from the corresponding author upon reasonable request.

References

Batini, F., Bertini, G., Bottai, A., Burgassi, P., Cappetti, G., Gianelli, G., Puxeddu, M., 1983. San Pompeo 2 deep well: a high temperature and high pressure geothermal system, in: Strub, A., Ungemach, P. (Eds.), European Geothermal Update: Proceedings of the 3rd International Seminar on the Results of EC Geothermal Energy Research, pp. 341–353.

Baron, G., Ungemach, P., 1981. European geothermal drilling experience—problem areas and case studies, in: International Geothermal Drilling and Completions Technology Conference. Albuquerque, NM, USA, p. 24.

Brudy, M., Zoback, M.D., 1999. Drilling-induced tensile wall-fractures: implications for determination of in-situ stress orientation and magnitude. Int. J. Rock Mech. Min. Sci. 36 (2), 191–215.

Cox, S.F., 2010. The application of failure mode diagrams for exploring the roles of fluid pressure and stress states in controlling styles of fracture-controlled permeability enhancement in faults and shear zones. Geofluids 10 (1–2), 217–233.

Elders, W.A., Friðleifsson, G., Albertsson, A., 2014. Drilling into magma and the implications of the Iceland Deep Drilling project (IDDP) for high-temperature geothermal systems worldwide. Geothermics 49, 111–118.

Ewy, R.T., Cook, N.G.W., 1990. Deformation and fracture around cylindrical openings in rock—I. Obervations and analysis of deformations. Int. J. Rock. Mech. Min. Sci. & Geomech. Abstr. 27 (5), 387–407.

Espinosa-Paredes, G., Garcia-Gutierrez, A., 2003. Estimation of static formation temperatures in geothermal wells. Energy Conv. Manag. 44 (8), 1343–1355.

Fournier, R.O., 1991. The transition from hydrostatic to greater than hydrostatic fluid pressure in presently active continental hydrothermal systems in crystalline rock. Geophys. Res. Lett. 18 (5), 955–958.

Friðleifsson, G.O., Albertsson, A., Stefansson, B., Gunnlaugsson, E., Adalsteinsson, H., 2007. Deep unconventional geothermal resources: a major opportunity to harness new sources of sustainable energy, in: Proceedings, 20th World Energy Conference, Rome. World Energy Council, p. 21.

Friðleifsson, G.O., Elders, W.A., 2005. The Iceland Deep Drilling project: a search for deep unconventional geothermal resources. Geothermics 34 (3), 269–285.

Friðleifsson, G.O., Elders, W.A., Albertsson, A., 2014. The concept of the Iceland Deep Drilling project. Geothermics 49, 2–8.

Friðleifsson, G.O., Elders, W.A., 2017. The Iceland Deep Drilling project geothermal well at Reykjanes successfully reaches its supercritical target. Geotherm. Resour. Counc. Bull. 46, 30–33.

Garcia, J., Hartline, C., Walters, M., Wright, M., Rutqvist, J., Dobson, P.F., Jeanne, P., 2016. The Northwest Geysers EGS demonstration project, California: Part 1: characterization and reservoir response to injection. Geothermics 63, 97–119.

Gholami, R., Moradzadeh, A., Rasouli, V., Hanachi, J., 2014. Practical application of failure criteria in determining safe mud weight windows in drilling operations. J. Rock Mech. Geotech. Eng. 6 (1), 13–25.

Goto, R., Watanabe, N., Sakaguchi, K., Miura, T., Chen, Y., Ishibashi, T., Pramudyo, E., Pariso, F., Yoshioka, K., Nakamura, K., Komai, T., Tsuchiya, N., 2021. Creating cloud-fracture network by flow-induced microfracturing in supercritical geothermal environments. Rock Mech. Rock Eng. 54, 2959–2974.

Griffith, A.A., 1924. Theory of rupture, in: Biezeno, C.B., Burgers, J.M. (Eds.), Proceedings of the First International Congress on Applied Mechanics. J Waltman, Delft, pp. 55–63.

Hiramatsu, Y., Oka, Y., 1968. Determination of the stress in rock unaffected by boreholes or drifts, from measured strains or deformations. Int. J. Rock Mech. Min. Sci. Geomech. Abstr. 5 (4), 337–353.

Hoek, E., Brown, E.T., 1980. Underground Excavations in Rock. The Institution of Mining and Metallurgy, London.

Jaeger, J.C., Cook, N.G.W., 1979. Fundamentals of Rock Mechanics, third ed. Chapman & Hall, London.

Kato, O., Doi, N., Sakagawa, Y., Uchida, T., 1998. Fracture systematics in and around well WD-1, Kakkonda geothermal field, Japan. Geothermics 27 (5–6), 609–629.

Kinoshita, N., Abe, T., Wakabayashi, N., Ishida, T., 1997. Mechanical properties of rock at high temperatures. Doboku Gakkai Ronbunshu 1997 (561), 151–162.

Kirsch, E.G., 1898. Die Theorieder Elastizit at unddie Bedurfnisse der Festigkeitslehre, Z. Ver. Dtsch. Ing. 42 (29), 797–807.

Lee, M., Haimson, B., 1993. Laboratory study of borehole breakouts in Lac du Bonnet granite: a case of extensile failure mechanism. Int. J. Rock Mech. Min. Sci. Geomech. Abstr. 30 (7), 1039–1045.

Morita, N., Nagano, Y., 2016. Comparative analysis of various failure theories for borehole breakout predictions. SPE Annual Technical Conference and Exhibition, Dubai, UAE. OnePetro.

Moore, D.E., Lockner, D.A., Byerlee, J.D., 1994. Reduction of permeability in granite at elevated temperatures. Science 265 (5178), 1558–1561.

Morrow, C.A., Moore, D.E., Lockner, D.A., 2001. Permeability reduction in granite under hydrothermal conditions. J. Geophys. Res. Solid Earth 106 (B12), 30551–30560.

Pariseau, W.G., 2009. Design Analysis in Rock Mechanics. Taylor and Francis, London.

Parisio, F., Vinciguerra, S., Kolditz, O. and Nagel, T., 2019. The brittle-ductile transition in active volcanoes. Sci. Rep. 9 (1), 1–10.

Parisio, F., Lehmann, C., Nagel, T., 2020. A model of failure and localization of basalt at temperature and pressure conditions spanning the brittle-ductile transition. J. Geophys. Res. Solid Earth 125 (11), e2020JB020539.

Ruggieri, G., Gianelli, G., 1995. Fluid inclusion data from the Carboli 11 well, Larderello geothermal field, Italy, in: World Geothermal Congress, Italy, pp. 1087–1091.

Saishu, H., Okamoto, A., Tsuchiya, N., 2014. The significance of silica precipitation on the formation of the permeable-impermeable boundary within earth's crust. Terra Nova 26 (4), 253–259.

Sakai, N., 1987. Mechanical behaviors of heated rocks under uniaxial compression, J. Jpn. Soc. Eng. Geol. 28 (1), 19–24.

Secor, D.T., 1965. Role of fluid pressure in jointing. Am. J. Sci. 263 (8), 633–646.

Song, I., Haimson, B.C., 1997. Polyaxial strength criteria and their use in estimating in situ stress magnitudes from borehole breakout dimensions. Int. J. Rock Mech. Min. Sci. 34 (3–4), 116.e1–116.e16.

Steingrimsson, B., Gudmundsson, A., Franzson, H., Gunnlaugsson, E., 1990. Evidence of a supercritical fluid at depth in the Nesjavellir field, in: Proceedings, 15th Workshop on Geothermal Reservoir Engineering. Stanford University, Stanford, p. 8.

Smith, R., Shaw, H., 1975. Igneous-related geothermal systems, in: White, D. Williams, D. (Eds.), Assessment of Geothermal Resources of the United States—1975. U.S. Geological Survey Circular 726, 58–83.

Smith, R., Shaw, H., 1979. Igneous-related geothermal systems, in: Muffler, L. (Ed.), Assessment of Geothermal Resources of the United States—1978. U.S. Geological Survey Circular 790, 12–17.

Tester, J.W., Anderson, B.J., Batchelor, A.S., Blackwell, D.D., DiPippo, R., Drake, E.M., Garnish, J., Livesay, B., Moore, M.C., Nichols, K., Petty, S., Toksöz, M.N., Veatch, Jr. R.W., 2006. The future of geothermal energy in the 21 century impact of enhanced geothermal systems (EGS) on the United States. MIT Press, Cambridge, MA.

Tsuchiya, N., Hirano, N., 2007. Chemical reaction diversity of geofluids revealed by hydrothermal experiments under sub- and supercritical states. Isl. Arc 16 (1), 6–15.

Tsuchiya, N., Yamada, R., Uno, M., 2016. Supercritical geothermal reservoir revealed by a granite-porphyry system. Geothermics 63, 182–194.

Tullis, J., Yund, R.A., 1977. Experimental deformation of dry Westerly granite. J. Geophys. Res. 82 (36), 5705–5718.

Violay, M., Heap, M.J., Acosta, M., Madonna, C., 2017. Porosity evolution at the brittle-ductile transition in the continental crust: implications for deep hydro-geothermal circulation. Sci. Rep. 7, 7705.

Watanabe, N., Abe, H., Okamoto, A., Nakamuraet, K., Komai, T., 2021. Formation of amorphous silica nanoparticles and its impact on permeability of fractured granite in superhot geothermal environments. Sci. Rep. 11, 5340.

Watanabe, N., Numakura, T., Sakaguchi, K., Saishu, H., Okamoto, A., Ingebritsen, S.E., Tsuchiya, N., 2017a. Potentially exploitable supercritical geothermal resources in the ductile crust. Nat. Geosci. 10 (2), 140–144.

Watanabe, N., Egawa, M., Sakaguchi, K., Ishibashi, T., Tsuchiya, N., 2017b. Hydraulic fracturing and permeability enhancement in granite from subcritical/brittle to supercritical/ductile conditions. Geophys. Res. Lett. 44 (11), 5468–5475.

Watanabe, N., Sakaguchi, K., Goto, R., Miura, T., Yamane, K., Ishibashi, T., Chen, Y., Komai, T., Tsuchiya, N., 2019. Cloud-fracture networks as a means of accessing supercritical geothermal energy. Sci. Rep. 9, 939.

Watanabe, N., Saito, K., Okamoto, A., Nakamura, K., Ishibashi, T., Saishu, H., Komai, T., Tsuchiya N., 2020. Stabilizing and enhancing permeability for sustainable and profitable energy extraction from superhot geothermal environments. Appl. Energy 260, 114306.

Weis, P., Driesner, T., Heinrich, C.A., 2012. Porphyry-copper ore shells form at stable pressure-temperature fronts within dynamic fluid plumes. Science 338 (6114), 1613–1616.

Zhao, Y., Feng, Z., Xi, B., Wan, Z., Yang, D., Liang, W., 2015. Deformation and instability failure of borehole at high temperature and high pressure in Hot Dry Rock exploitation. Renewable energy 77, 159–165.

Zoback, M.D., Moos, D., Mastin, L., Anderson, R.N., 1985. Well bore breakouts and in situ stress. J. Geophys. Res. 90 (B7), 5523–5530.

Wellbore stability in high-temperature granite under true triaxial stress

Ryota Goto[a], Kiyotoshi Sakaguchi[a], Francesco Parisio[b], Keita Yoshioka[c], Eko Pramudyo[a], Noriaki Watanabe[a,*]

[a] Department of Environmental Studies for Advanced Society, Graduate School of Environmental Studies, Tohoku University, Sendai 9808579, Japan

[b] Chair of Soil Mechanics and Foundation Engineering, Technische Universitaet Bergakademie Freiberg, Freiberg 09599, Germany

[c] Department of Environmental Informatics, Helmholtz Centre for Environmental Research–UFZ, Leipzig 04318, Germany

*Corresponding author. E-mail address: noriaki.watanabe.e6@tohoku.ac.jp, Tel & Fax: +81-22-795-7384

Abbreviations: AE, acoustic emissions

Abstract

Supercritical/superhot geothermal success depends on successful drilling. However, wellbore stability in supercritical environments has not been investigated because imposing sufficient stress on high-temperature granite with true triaxial loading is difficult. We conducted wellbore failure experiments on 200–450 °C granite under true triaxial stress, including deformation and acoustic emission measurements, and post-experiment thin section observations. Wellbore failure initiated at stress states consistent with existing brittle failure criterion at the studied temperatures. Using breakout geometry for *in situ* stress estimation may be difficult as shear failure propagation is suppressed at high temperatures; however, boreholes may be inherently stable in high-temperature environments.

Keywords: wellbore failure, granite, high temperature, supercritical geothermal environment, superhot geothermal environment, true triaxial stress

1. Introduction

Recent attention in geothermal power generation has focused on methods for harvest geothermal energy from unconventional supercritical (or superhot) geothermal environments that exceed the critical temperature of water (374 °C for pure water and 406 °C for seawater) at drillable depths of approximately 2–4 km, as found in Iceland (Friðleifsson et al., 2014; Friðleifsson and Elders, 2017; Steingrimsson et al., 1990), Italy (Baron and Ungemach, 1981; Batini et al., 1983; Ruggieri and Gianelli, 1995), Japan (Kato et al., 1998), Mexico (Espinosa-Paredes and Garcia-Gutierrez, 2003), and the United States (Fournier, 1991; Garcia et al., 2016). Supercritical geothermal environments can provide superheated steam or supercritical water with an extremely high specific enthalpy exceeding 2 MJ/kg (Elders et al., 2014; Friðleifsson and Elders, 2005; Friðleifsson et al. 2007; Smith and Shaw, 1975, 1979; Tester et al., 2006). Therefore, harvesting supercritical geothermal energy is expected to increase the productivity and sustainability of geothermal energy generation. However, in supercritical geothermal environments on the continental crust, the formation of permeable fracture networks (Tsuchiya et al., 2016; Watanabe et al., 2017a; Weis et al., 2012) can potentially be suppressed by the increased efficiency of mineral crystal plasticity (Parisio et al., 2019, 2020; Tullis and Yund, 1977; Violay et al., 2017), the retrograde solubility of silica minerals (Fournier, 1991; Saishu et al., 2014; Tsuchiya and Hirano, 2007; Watanabe et al., 2021), and the enhanced rates of fracture healing/sealing caused by water–rock reactions (Moore et al., 1994; Morrow et al., 2001; Watanabe et al., 2020). Therefore, it is necessary to develop enhanced geothermal system technologies to artificially create or recreate permeable fracture networks in these supercritical geothermal environments.

Recent studies have suggested that the injection of water at or near its critical temperature into granite is likely to create a dense network of microfractures suitable for geothermal energy extraction, a so-called cloud-fracture network, through continuous infiltration and the stimulation of pre-existing microfractures by the low-viscosity water (Goto et al. 2021; Watanabe et al., 2017b, 2019). Additionally, it has been suggested that the pore pressure required to initiate this flow-induced microfracturing may be well predicted by the Griffith failure criterion, which assumes the initiation of brittle failure from pre-existing fractures and is a function of the maximum and minimum principal stresses and tensile strength of rocks (Cox, 2010; Griffith, 1924; Jaeger and Cook, 1979; Secor, 1965). However, the characteristics of wellbore failure (Ewy and Cook, 1990; Morita and Nagano, 2016), and the possibility of utilizing these failures (i.e., induced fractures and breakout) for in situ stress estimation (Brudy and Zoback, 1999; Kato et al., 1998; Zoback et al., 1985) to achieve safe and effective fracturing at the minimum required injection pressure, remain unclear for supercritical geothermal environments. This is because wellbore failure experiments under true triaxial stress (Lee and Haimson, 1993; Song and Haimson, 1997) have never been conducted on high-temperature granite. To the best of our knowledge, wellbore failure experiments under hydrostatic stress have only been conducted on granite at temperatures up to 600 °C (Zhao et al., 2015).

The aim of this study is to experimentally simulate wellbore failure in granite under true triaxial stress in supercritical geothermal conditions. We first introduce a novel experimental method for assessing high-temperature wellbore failure in relatively large (10-cm cubic) rock samples under true triaxial stress. Subsequently, we present the results of experiments conducted on granite at 200–450 °C, which show non-catastrophic wellbore failure. Finally, we suggest the predictability of the initiation of wellbore failure using an existing failure criterion for rocks and discuss the possibility of estimating in situ stress from wellbore failure.

2. Experimental methods

2.1. Granite and experimental system

Cubes (100 × 100 × 100 mm) of Inada granite from Ibaraki prefecture, Japan (Figure 1), with a single wellbore (diameter: 10 mm, length: 100 mm) at the center, were prepared for the high-temperature wellbore failure experiment under true triaxial stress. Inada granite, of which the porosity at room temperature and atmospheric pressure is 0.5-0.8%, has been used in previous studies on supercritical hydraulic fracturing (Goto et al., 2021; Watanabe et al., 2017b, 2019).

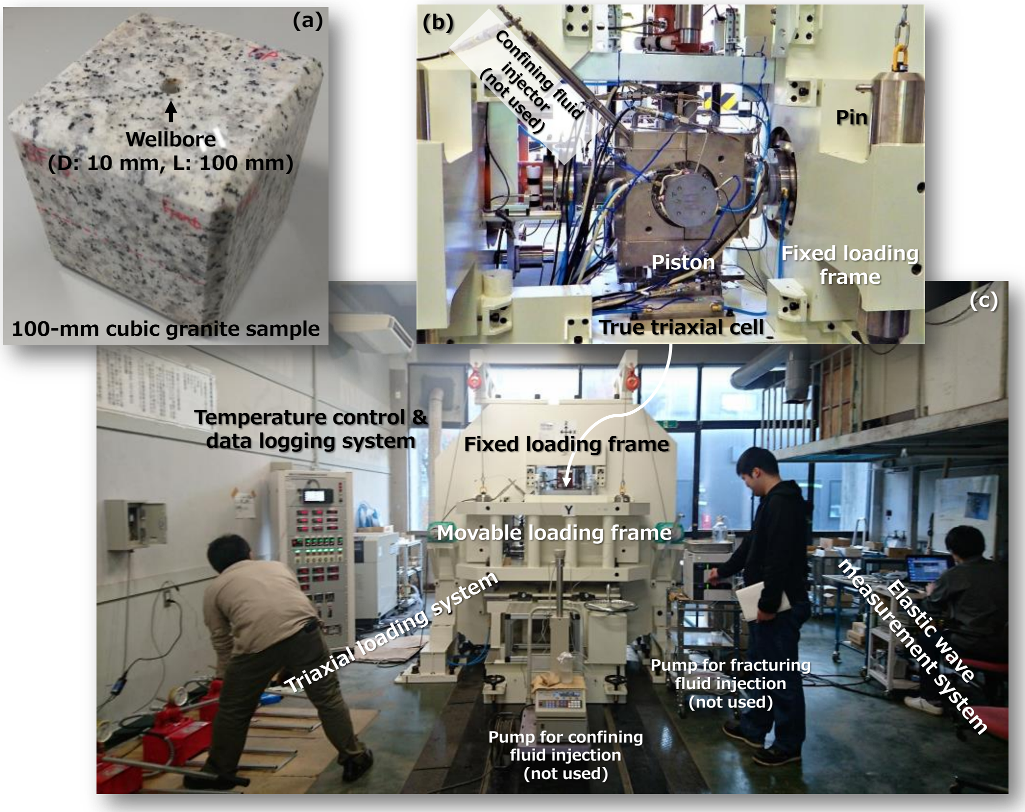

Figure 1. Granite sample (a), high-temperature true triaxial cell (b), and experimental system (c) in the wellbore failure experiment, adapted from Watanabe et al. (2019).

We used the experimental system (Figure 1) originally developed for supercritical hydraulic fracturing by Watanabe et al. (2019) and applied in Goto et al. (2021). The system consisted of a true triaxial cell, a triaxial loading system, a pump for injecting fracturing fluid into the sample, a pump for injecting confining fluid (high-viscosity plastic melt in this system) along the sample edges via an injector, an elastic wave measurement system, and a temperature control and data logging system. In the present experiment, the elastic wave measurement system was an acoustic emission (AE) measurement device (Physical Acoustics Cooperation's two-channel data acquisition and digital signal processing AE system, PCI-2), and the pumps and injector were not used because no fracturing or confining fluids were required for the experiment.

The true triaxial cell (Figure 2) consisted of a pressure vessel with a cubic skeleton, six pistons to apply a compressive load to the 100 × 100 × 100 mm cubic rock sample via a stainless-steel plate (for better mechanical coupling between the piston loading faces and the sample), and thermal insulators used in conjunction with heaters for the pressure vessel. The pressure vessel had six cylindrical holes to allow the pistons to be inserted into the vessel, with graphite packing lubricating the sliding portions. The edges of the sample were chamfered so that the loading face of the sample had 90 mm sides that corresponded to the shape (i.e., 90 × 90 mm) of both the loading face of the piston and the stainless-steel plate. Each piston was equipped with four cartridge heaters and a pipe through which a thermocouple could reach the vicinity of the sample surface, and had an elastic wave guide bar on the opposite side of the loading face. An AE sensor (R15α, 150-kHz resonant frequency sensor, Physical Acoustics Corporation) was attached to the face of the elastic wave guide bar, while two AE sensors were used for one pair of the opposed horizontal pistons, where these pitons were used to apply the far-field maximum horizontal stress described in section (2.2). The temperature of the bar was maintained near ambient conditions using a cooling jacket through which water from a chiller circulated.

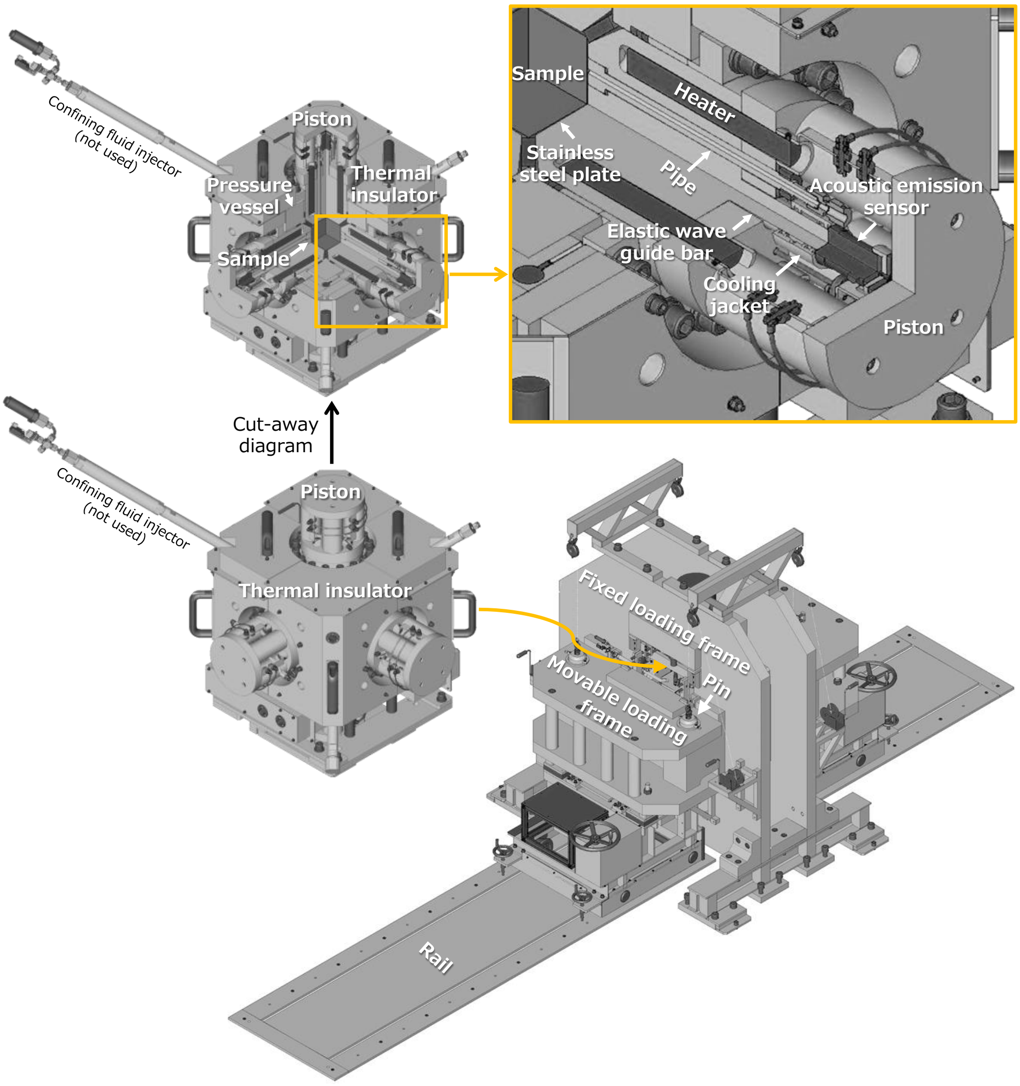

Figure 2. Three-dimensional design of the high-temperature true triaxial cell and triaxial loading frame, adapted from Watanabe et al. (2019).

The triaxial loading system (Figure 2) comprised a fixed loading frame and a movable loading frame. The fixed frame had two hydraulic rams that were placed vertically and horizontally. The movable loading frame contained a horizontal hydraulic ram. Each hydraulic ram had a capacity of 3 MN and was actuated using a manual oil pump. The true triaxial cell was placed on the loading platform of the fixed frame extremely carefully to prevent any loading eccentricity. It was then connected to the AE measurement system and the temperature control and data logging system. When a compressive load was applied, the movable loading frame engaged with the fixed loading frame via four cylindrical pins.

The triaxial loading system independently applied compressive loads in three orthogonal directions, using a single hydraulic ram with a fixed loading platen on the opposite side. The hydraulic ram, equipped with a load cell, pushed the piston of the true triaxial cell via a spherical seated platen. The displacement of the piston was ascertained as a proxy for sample deformation, using a linear variable differential transformer displacement transducer. The displacement transducer was attached to a cantilever attached to the fixed loading platen side, so that the measured displacement excluded any expansion between opposing platens caused by loading frame deformation in response to large loads.

2.2. Experimental procedures and conditions

The first procedure involved increasing the temperature of the pressure vessel and pistons to a prescribed value (200, 350, or 450 °C) while a hydrostatic load (approximately 1 MPa) was applied to a sample with a vertical wellbore. Once the temperature reached the prescribed value, the sample was subjected to an initial stress state with a hydrostatic pressure of 53 MPa. To induce wellbore failure, one of the horizontal stresses, referred to as the far-field minimum horizontal stress (σ_h) in this study, was then decreased continuously and gradually to approximately 5 MPa by returning oil to the manual oil pump, while the far-field maximum horizontal stress (σ_H) and the vertical stress (σ_V) remained constant at the initial level. The manual oil pump was equipped with a flow control valve so that the load could be continuously decreased by returning oil to the pump using a constant valve opening.

For post-mortem analysis, the sample was impregnated with a thermosetting acrylic resin under vacuum conditions and then heated to 50 °C under atmospheric pressure, so that the cured resin preserved structural changes within the sample. The resin-impregnated sample was cut horizontally across the middle region containing the wellbore, and a thin section of the inner region was prepared to assess wellbore failure via optical microscopy.

Based on Kirsch's equations (Gholami et al., 2014; Hiramatsu and Oka, 1968; Kirsch, 1898), the state of stress around the wellbore in isotopic elastic homogenous rocks in a cylindrical coordinate system (r, θ, z), for which r (from the center of the wellbore), θ (from the σ_H direction), and z correspond to the radial, tangential, and axial (vertical) directions of the wellbore, respectively, may be estimated as follows:

$$\sigma_r = \frac{1}{2}(\sigma_H + \sigma_h)\left(1 - \frac{R^2}{r^2}\right) + \frac{1}{2}(\sigma_H - \sigma_h)\left(1 - \frac{4R^2}{r^2} + \frac{3R^4}{r^4}\right)\cos(2\theta) + P_w\frac{R^2}{r^2}, \quad (1)$$

$$\sigma_\theta = \frac{1}{2}(\sigma_H + \sigma_h)(1 + \frac{R^2}{r^2}) - \frac{1}{2}(\sigma_H - \sigma_h)(1 + \frac{3R^4}{r^4})\cos(2\theta) - P_w\frac{R^2}{r^2}, \text{ and} \quad (2)$$

$$\sigma_z = \sigma_V - 2\nu(\sigma_H - \sigma_h)\cos(2\theta), \quad (3)$$

where σ_r, σ_θ, and σ_z are the radial, tangential, and axial stresses, respectively, R is the radius of the wellbore, Pw is the internal wellbore pressure, and ν is the Poisson's ratio, where P_w is assumed to be zero for the experiments under dry condition in this study. Notably, the applicability of Kirsch's equations on a wellbore in the granite used in the present study has been previously confirmed via a hydraulic fracturing experiment on the same granite (diameter: 30 mm, length: 25 mm) with a wellbore (diameter: 1.5 mm, length: 10 mm) (Watanabe et al., 2017b).

Based on the Hoek–Brown failure criterion, a well-known empirical wellbore failure surface (Hoek and Brown, 1980; Pariseau, 2009) is represented by

$$(\sigma_1 - \sigma_3)^2 - (A\sigma_3 + B^2) = 0, \quad (4)$$

$$A = \frac{\sigma_c^2 - \sigma_t^2}{\sigma_t}, \text{ and} \quad (5)$$

$$B = \sigma_c, \quad (6)$$

where σ_1, σ_2, and σ_3 are the maximum, intermediate, and minimum principal stresses, respectively, and σ_c and σ_t are the unconfined compressive and tensile strengths, respectively.

According to the literature, the σ_c of the granite used in this study is approximately 150 MPa at 200 °C, 130 MPa at 350 °C, and 120 MPa at 450 °C (Sakai, 1987), while the σ_t and ν of the same granite remain relatively constant across the range of experimental temperatures, approximately 6 MPa and 0.2, respectively (Kinoshita et al., 1997). Using these values, the Hoek–Brown failure criterion provides the following predictions regarding the initiation of tensile and shear failures at $\theta = 0°$ and 90° for the wellbore (Figure 3). Tensile failure, which may produce tensile fractures, by increasing the σ_θ under tension at $\theta = 0°$ starts at the same σ_h level at all temperatures because σ_t is temperature-independent. In contrast, shear failure, which may cause breakout, by increasing the σ_θ under compression at $\theta = 90°$ is initiated at higher σ_h values (i.e., smaller σ_θ) at higher temperatures, because of the smaller σ_c. Table 1 lists these estimated and predicted values. According to our computations, we expect non-catastrophic failure producing millimeter-scale breakout and/or tensile fractures, because the significantly increased σ_θ in both the compression and tension is contained to within 10 mm of the wellbore under the final state of far-field stress (Eq. 2).

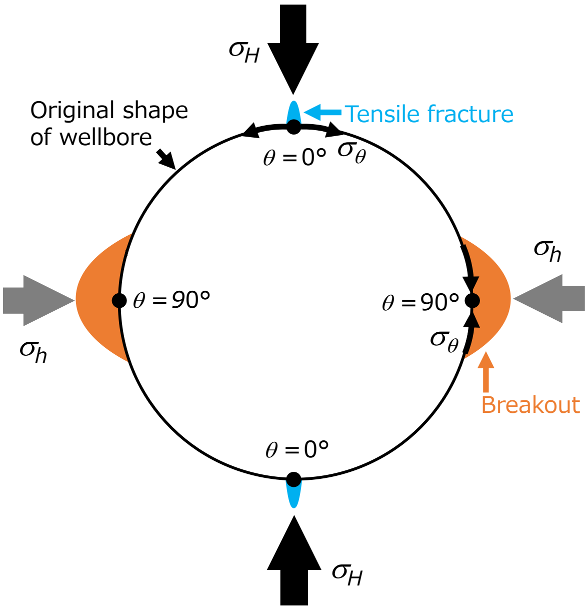

Figure 3. Conceptual illustration of breakout and tensile fractures in the wellbore wall, caused by shear and tensile failures, respectively.

Table 1. Estimated unconfined compressive and tensile strengths (σ_c and σ_t) and predicted far-field minimum horizontal stress (σ_h) for shear and tensile failures at each experimental temperature.

Temperature (°C)	σ_c (MPa)	σ_t (MPa)	σ_h at failure (MPa)	
			Shear failure	Tensile failure
200	150	6	6	15
350	130	6	26	15
450	120	6	36	15

3. Results and discussion

3.1. Temporal changes in stress, resultant behaviors of displacement and AE

Figures 4–6 show temporal changes in the far-field stresses (σ_h, σ_H, and σ_V) and corresponding changes in the estimated stresses on the wellbore (σ_θ and σ_z) using Eqs. 2 and 3, the displacement of the piston (a proxy of sample deformation) in the σ_H and σ_V directions, and the AE energy with its cumulative value, for the three experiments at 200, 350, and 450 °C. In the AE measurement device used in this study, AE energy is calculated as the time integral of the absolute signal voltage and reported in arbitrary units (a.u.). AE energy shown herein is the sum of the values obtained from the two AE sensors; we conducted the experiment at 450 °C, twice, and confirmed the absence of significant large AE energy in the second experiment (i.e., after failure in the first experiment) as illustrated in Supplementary Figure S1.

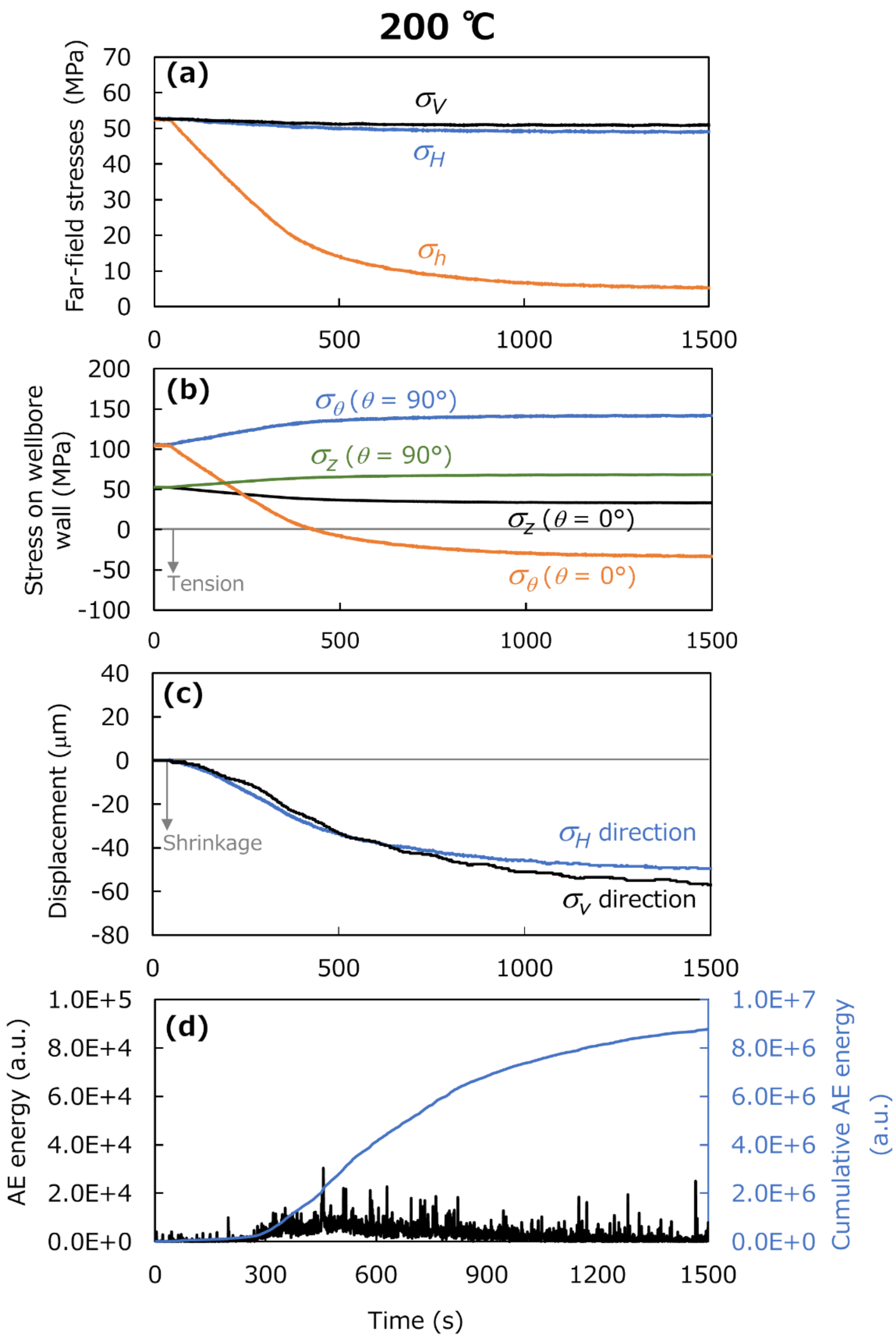

Figure 4. Temporal changes in the far-field stresses (a) and corresponding changes in the estimated stresses on the wellbore wall (b), displacement of the piston (c), and acoustic emission (AE) energy and its cumulative value (d), in the experiment at 200 °C.

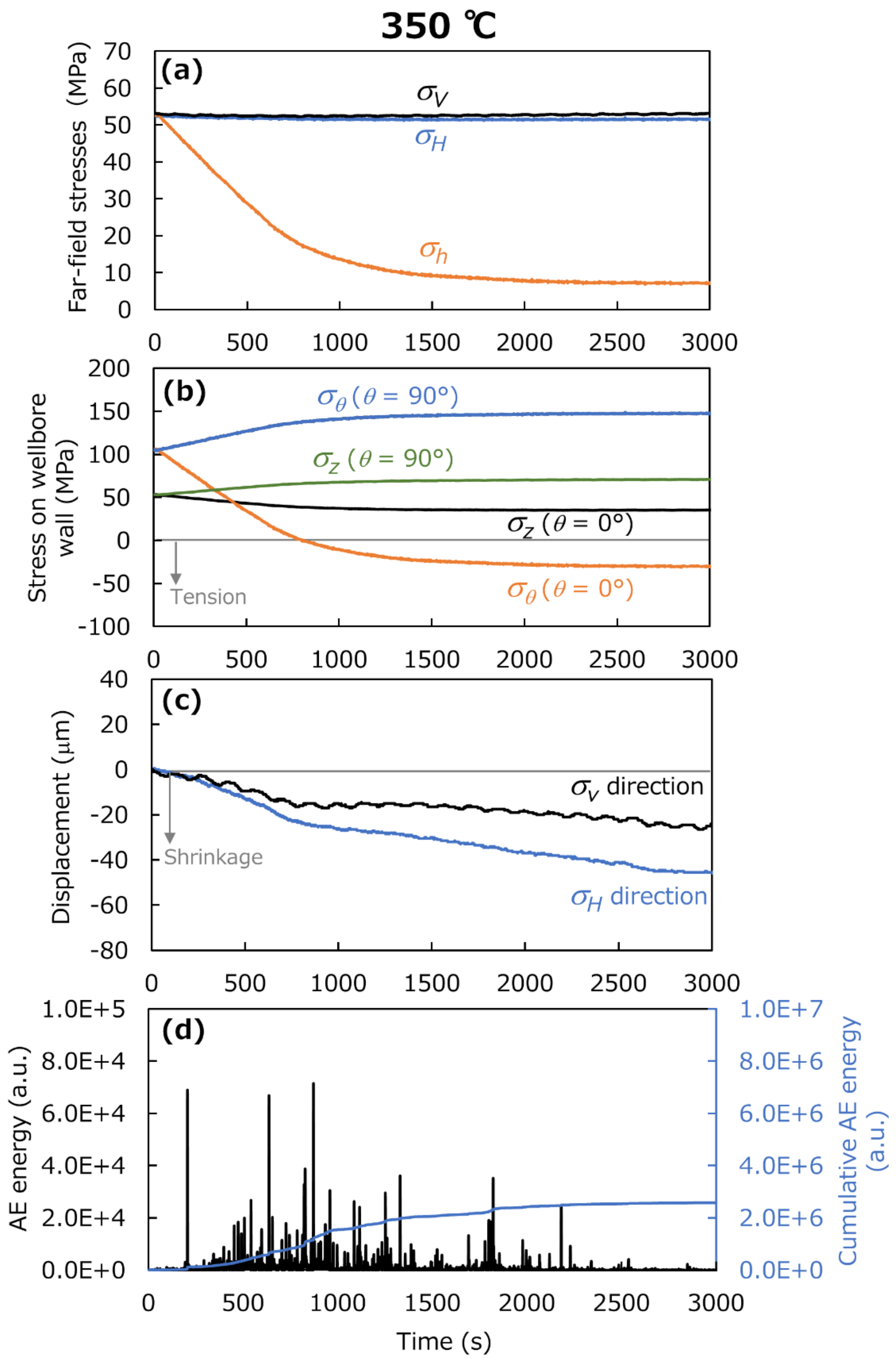

Figure 5. Temporal changes in the far-field stresses (a) and corresponding changes in the estimated stresses on the wellbore wall (b), displacement of the piston (c), and acoustic emission (AE) energy and its cumulative value (d), in the experiment at 350 °C.

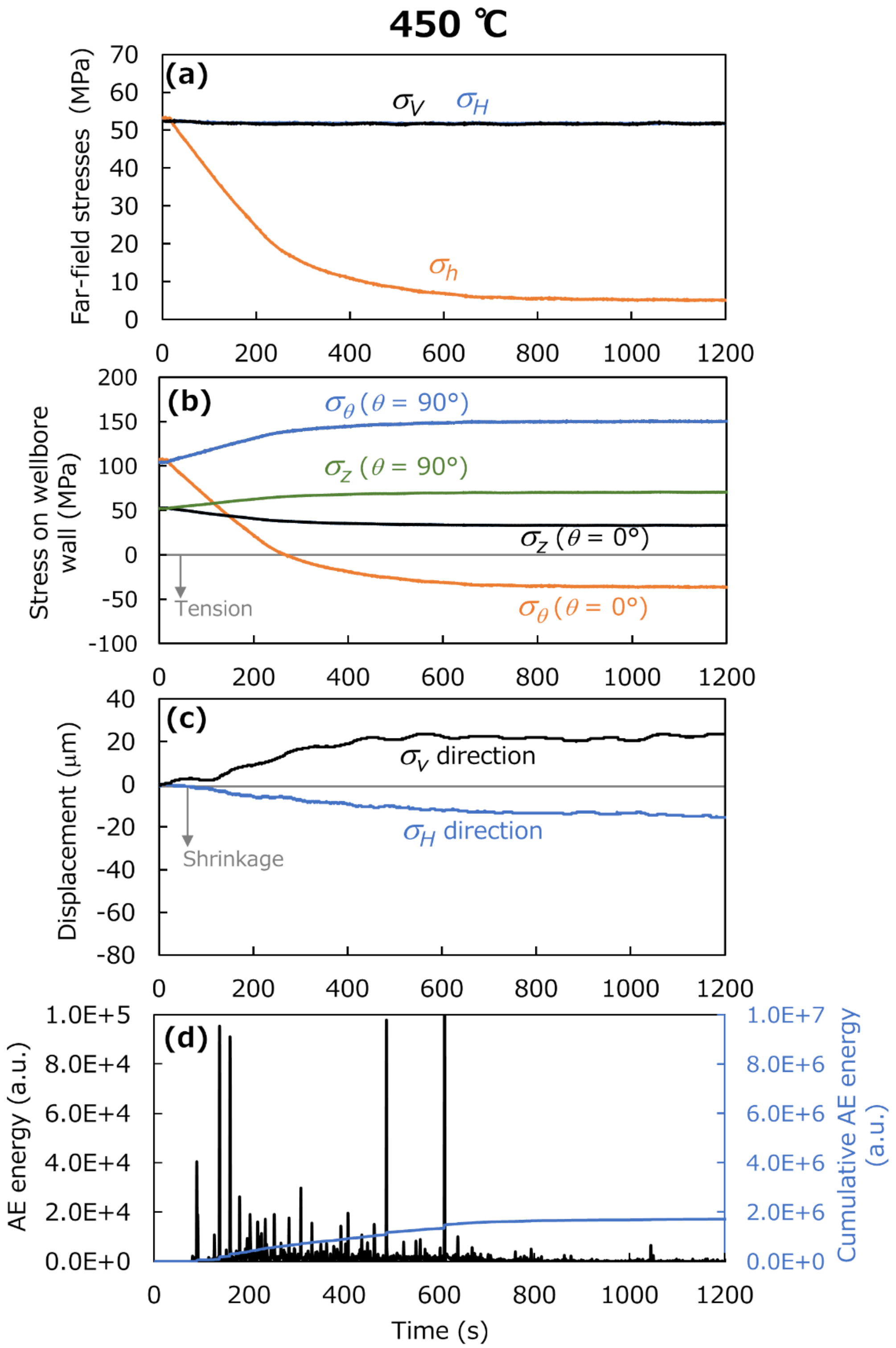

232

233 Figure 6. Temporal changes in the far-field stresses (a) and corresponding changes in the

234 estimated stresses on the wellbore wall (b), displacement of the piston (c), and acoustic

235 emission (AE) energy and its cumulative value (d), in the experiment at 450 °C.

236

In all the experiments, we were able to decrease σ_h smoothly up to approximately 5 MPa by transferring the oil back to the manual oil pump, while σ_V and σ_H remained almost constant. The rate of σ_h change was faster for higher σ_h (oil pressure) because the flow control valve opening was kept constant (Figures 4a, 5a, and 6a). The rate of σ_h decline in the experiment at 350 °C was slower than those in the other two experiments because it was conducted at a lower room temperature in winter, which affected the oil viscosity. The final σ_h level in each experiment exceeded the predicted criteria for shear failure (6–36 MPa at 450–200 °C) and/or tensile failure (15 MPa at all temperatures) of the wellbore (Table 1). σ_θ and σ_z also changed nonlinearly in response to nonlinear changes in σ_h (Figures 4b, 5b, and 6b). At $\theta = 0°$ (θ as defined in Figure 3), σ_θ decreased to −30 to −40 MPa (i.e., 30–40 MPa in tension), whereas at $\theta = 90°$, σ_θ increased to approximately 140–150 MPa.

Although the final σ_h in each experiment exceeded the predicted criteria for the shear failure and/or tensile failure of the wellbore, the changes in displacement (Figures 4c, 5c, and 6c) and cumulative AE energy (Figures 4d, 5d, and 6d) in all experiments were continuous before reaching a plateau, suggesting non-catastrophic shear and tensile failures, as illustrated in Figure 3. The displacement data at 200 °C indicate that the sample shrank similarly in both the σ_H and σ_V directions with decreasing σ_h. With increasing temperature, the sample shrank less in the σ_V and/or σ_H directions, and it dilated in the σ_V direction at 450 °C. Additionally, we observed that the AE energy behavior changed with increasing temperature. For low temperatures, we recorded smaller AE energies frequently. In contrast, at high temperatures, higher AE energies were recorded infrequently, resulting in a lower cumulative AE energy. These changes in displacement and AE behavior with increasing temperature may have been caused by the predicted shift in the predominant failure mode of the wellbore from tensile to shear failure (Table 1).

3.2. Wellbore failure prediction

Figures 7–9 show the changes in the displacement of the piston and AE energy as a function of σ_h in each experiment, together with the predicted σ_h for the shear and tensile failure of the wellbore. Although the sample shrank continuously in both the σ_H and σ_V directions throughout the experiment at 200 °C, the shrinkage accelerated when the loading reached the predicted tensile failure threshold (the stress path is indicated by the green arrow in Figure 7a). Additionally, we recorded large AE energy events, as indicated by the blue arrow, when σ_h reached the predicted tensile failure threshold (Figure 7b). This suggests that the tensile failure of the wellbore started around the expected σ_h level and tensile fractures were generated in the σ_V–σ_H plane, as illustrated in Figure 3, meaning that the sample deformed more easily in the σ_V and σ_H directions. We recorded another set of large AE energy events, as indicated by the red arrow, around the predicted shear failure threshold. However, after the presumed tensile failure, the stress field was altered and the initial shear failure prediction may no longer have been valid. Indeed, the displacement behavior did not change, despite the second set of large AE energy events.

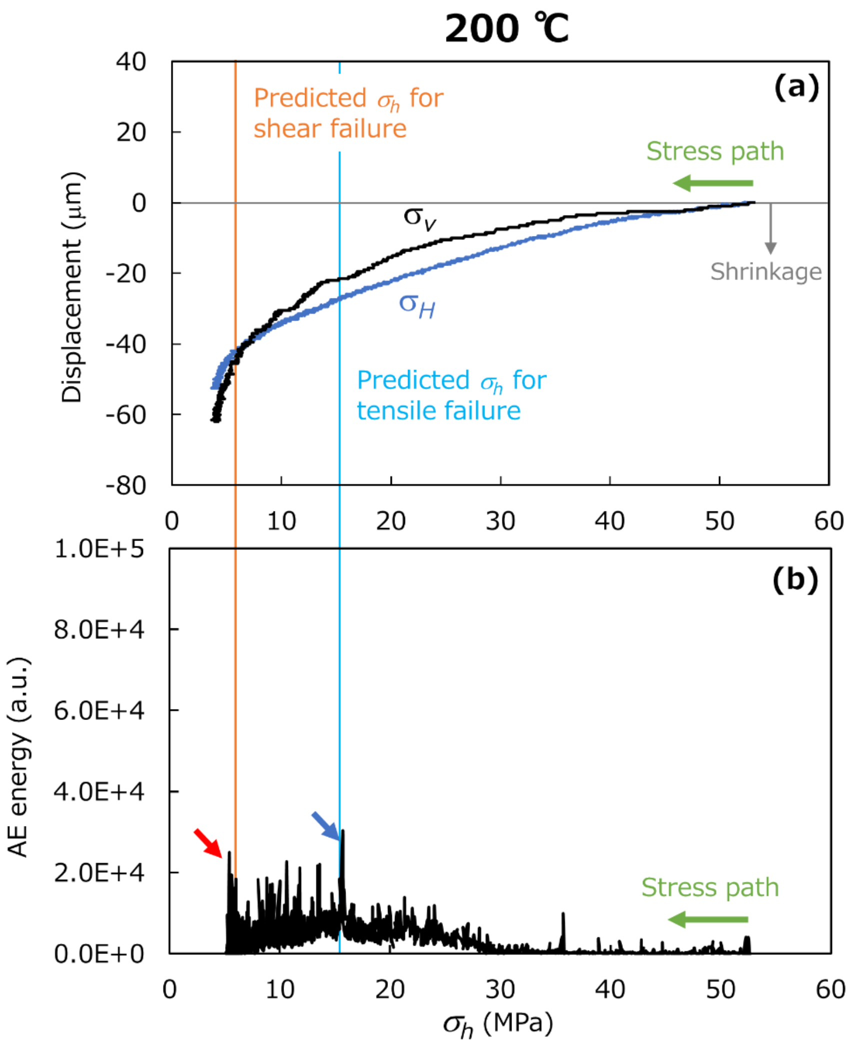

Figure 7. Changes in the displacement of the piston (a) and acoustic emission (AE) energy (b) as a function of σ_h in the experiment at 200 °C, together with the predicted σ_h for the shear and tensile failure of the wellbore wall.

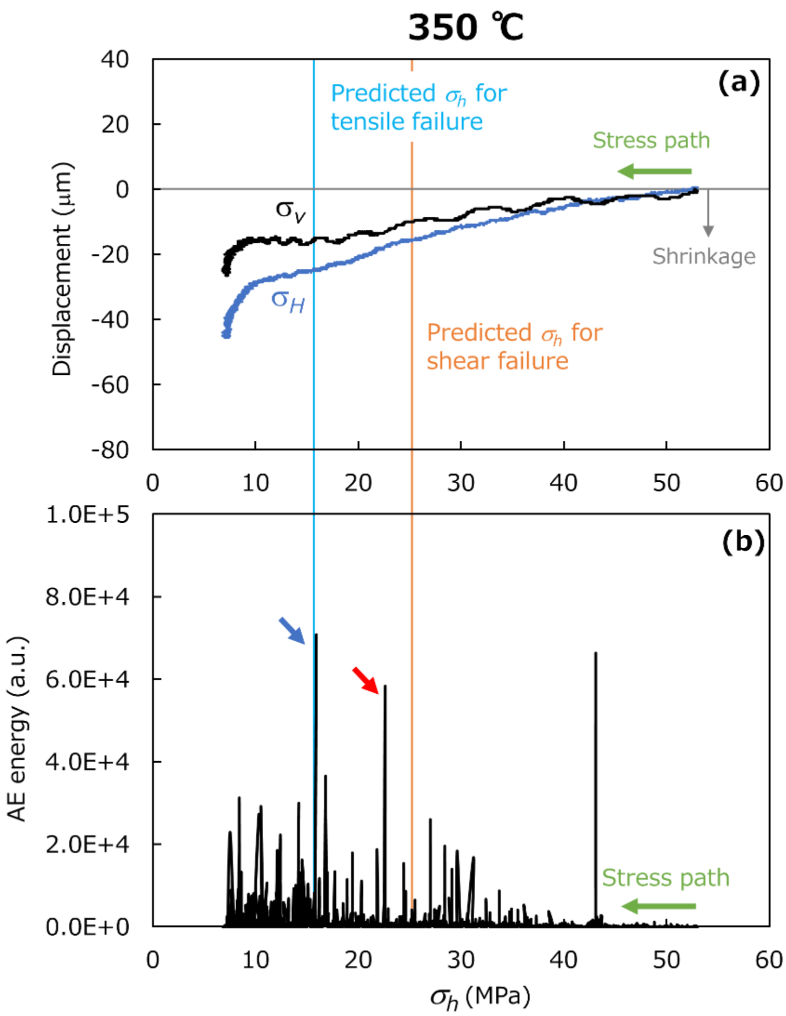

Figure 8. Changes in the displacement of the piston (a) and acoustic emission (AE) energy (b) as a function of σ_h in the experiment at 350 °C, together with the predicted σ_h for the shear and tensile failure of the wellbore wall.

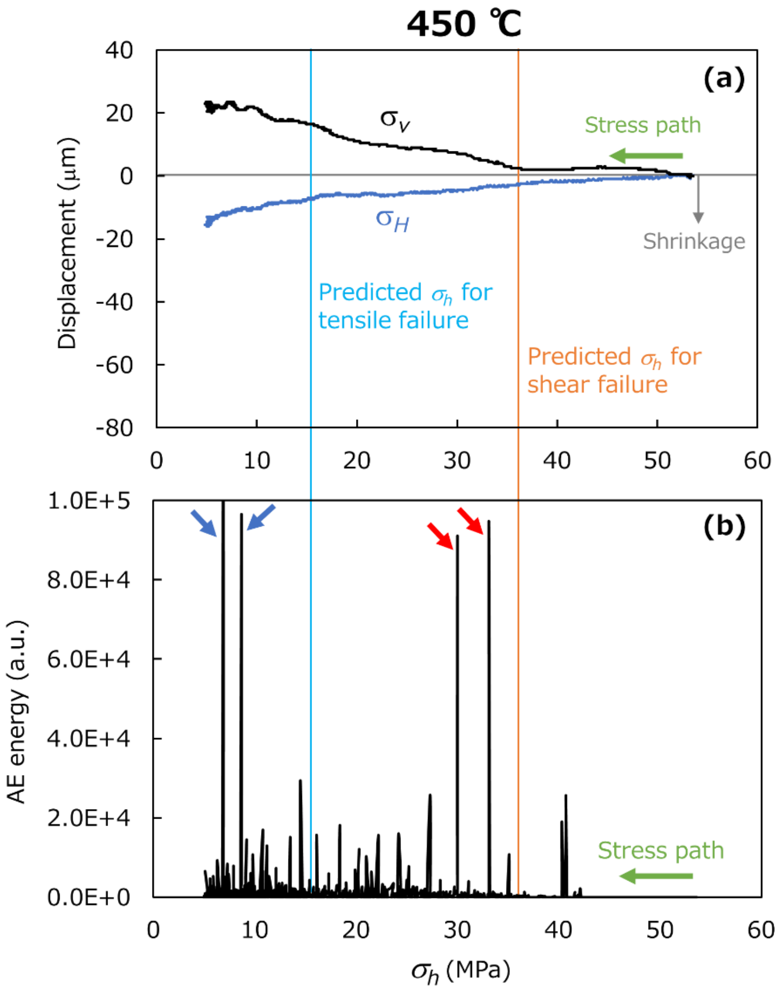

Figure 9. Changes in the displacement of the piston (a) and acoustic emission (AE) energy (b) as a function of σ_h in the experiment at 450 °C, together with the predicted σ_h for the shear and tensile failure of the wellbore wall.

In contrast, at 450 °C, significant dilation in the σ_V direction started after the predicted shear failure loading (Figure 9a) and large energy AE events occurred, as indicated by the red arrows in Figure 9b. This suggests the occurrence of wellbore shear failure that caused dilation in the σ_V direction, as Zhao et al. (2015) observed shear failure and increased axial deformation in a wellbore in granite under hydrostatic stress. After the predicted tensile failure, remarkably large energy AE events occurred again, as indicated by the blue arrows in Figure 9b. However, the second set of large energy AE events occurred at a much smaller σ_h than the predicted value for tensile failure, and there was no clear indication of tensile failure in the deformation behavior. This suggests that shear failure dominated the wellbore failure throughout the experiment at 450 °C.

In the 350 °C experiment (Figure 8), after the sample reached the predicted shear failure, the σ_h-dependence of the shrinkage in the σ_V direction decreased, flattening the displacement curve at an σ_h of approximately 10–20 MPa. Based on the discussion of the 450 °C experiment, this change in displacement behavior can be attributed to shear failure inducing dilation in the σ_V direction. Subsequently, at σ_h < 10 MPa, the σ_h-dependence of the shrinkage in both the σ_V and σ_H directions increased. Based on the discussion of the 200 °C experiment, this can be attributed to tensile failure inducing shrinkage in both the σ_V and σ_H directions. Indeed, we recorded large AE energies, as indicated by the red and blue arrows, around the predicted shear and tensile failures. This suggests that, at 350 °C, both shear and tensile failure significantly contributed to wellbore failure, owing to their relatively similar σ_h levels.

The above discussion suggests that the wellbore failure in the present experiments occurred at σ_h levels that were largely consistent with the predicted values (Table 1). Therefore, it is possible to predict wellbore failure in supercritical geothermal environments based on existing rock failure criterion, such as the Hoek–Brown criterion used in this study.

3.3. Possibility of using wellbore failure for in situ stress estimation

Figure 10 shows optical microphotographs of the thin sections prepared from the samples after the experiment (Figure 10a–c) and from an intact sample, for comparison, which was not used in any experiment (Figure 10d). In these microphotographs, the profile of the wellbore is traced in red, whereas the yellow line indicates a perfect circle

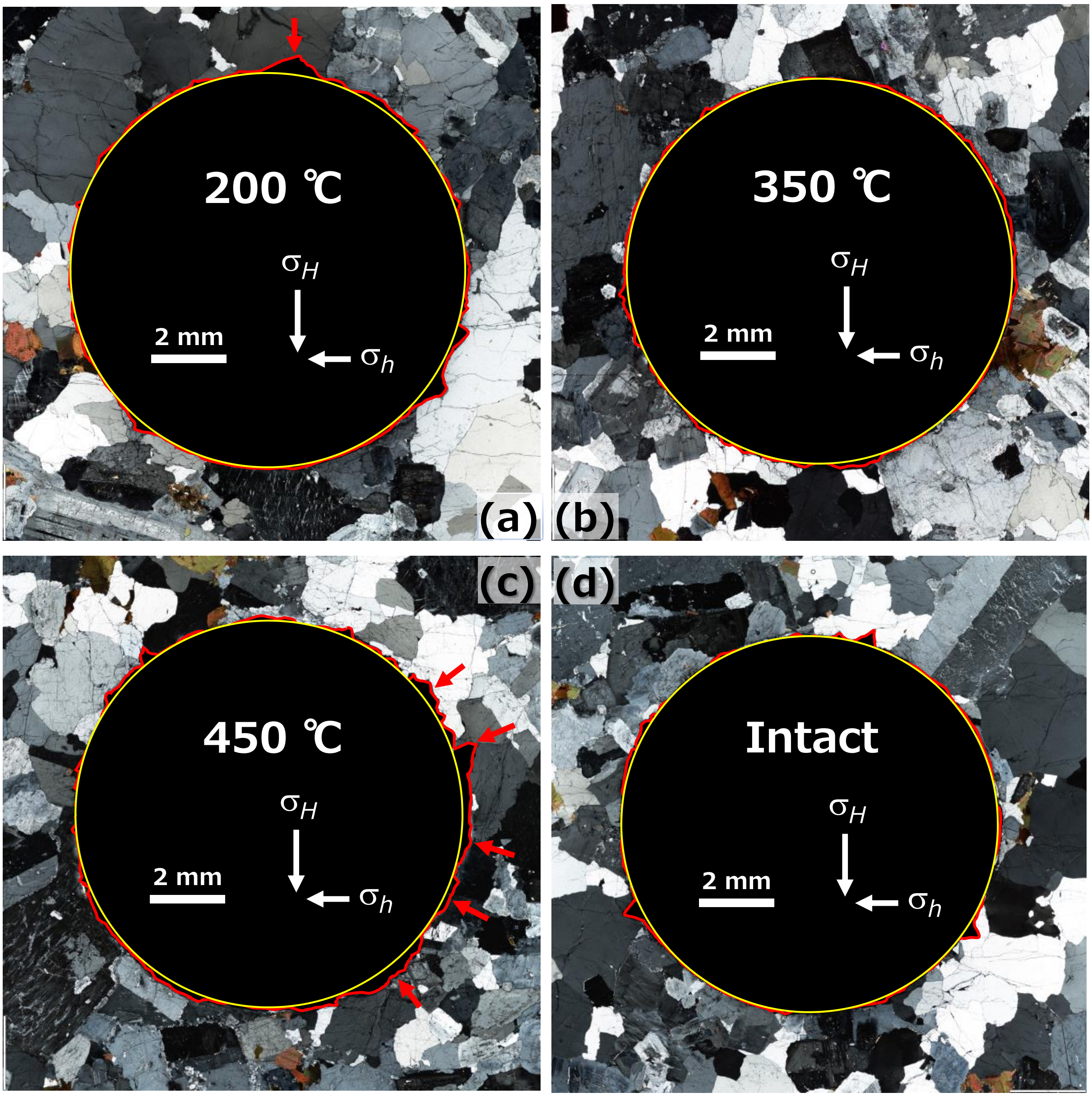

Figure 10. Optical microphotographs of thin sections prepared from the samples after the experiments at 200 (a), 350 (b), and 450 °C (c), and from an intact sample for comparison (d).

Even the intact sample profile does not completely match the perfect circle because of the relatively small defects with acute triangular shapes caused by boring (Figure 10d). However, the 200 °C profile deviates more from the perfect circle owing to the presence of larger defects in the wellbore, as indicated by the red arrow in Figure 10a. The largest defect appears to be a tensile fracture produced by the dominant failure at 200 °C (i.e., tensile failure at θ = 0° in Figure 3). The 450 °C profile also deviated significantly from the perfect circle owing to the presence of much broader defects, as indicated by the red arrows (Figure 10c). The defects appear to be breakouts produced by the dominant failure at 450 °C (i.e., shear failure at θ = 90° in Figure 3). The changes in the wellbore shape are consistent with our speculation that the dominant failure mode shifts from tensile (200 °C) to shear (450 °C). In contrast, the 350 °C profile did not significantly deviate from the perfect circle, although small deviations appear around the entire wellbore wall (Figure 10b). It would therefore be reasonable to assume no clear defects at specific locations if, as suggested in the previous section (3.2), both shear and tensile failure significantly contributed to the wellbore failure at 350 °C.

The present experimental results therefore suggest that breakout and tensile fractures may occur in wellbores in supercritical geothermal environments. However, at either 350 °C or 450 °C, we did not observe the textbook breakout shape (Figure 3), such as the shape observed in previous studies on granite at room temperature (Lee and Haimson, 1993; Song and Haimson, 1997). This suggests that high temperatures suppress the propagation of shear failure and its formation of clear breakout patterns. This may have been related to the intermittent large energy AE events at 350 and 450 °C (Figures 5d and 6d), because such intermittent large AE events were not observed in the previous study (Lee and Haimson, 1993). This, in turn, suggests that in situ stress estimation from the shape of the breakout would be difficult in supercritical geothermal environments because of the suppression of failure propagation at high temperatures. However, if shear failure propagation is suppressed and wellbore failure does not propagate further into the formation at high temperatures, this would greatly improve wellbore stability and suggests the possibility of underbalanced drilling, which would substantially reduce the risk of circulation loss during drilling. If our conclusions are correct, they would have tremendous implications for drilling practices in supercritical geothermal development. The suppressed failure propagation from the wellbore wall into the rock may have been caused by a rapid relaxation of stress concentration around the wellbore since several points on the circumference of the wellbore wall simultaneously reached failure, or became close, due to the relatively small unconfined compressive strength. However, this was not confirmed, hence warrants further investigation. Thus, extensive future studies are encouraged to examine the suppression of failure propagation at high temperatures and to clarify the mechanisms involved. Ideally, such studies should address wellbore failure in high-temperature granite along the temperature and stress paths that may occur during drilling, with considerations on influences of fluid pressure and thermal stress as well as *in situ* preexisting weakness planes.

4. Conclusions

For the successful development of enhanced geothermal systems in supercritical geothermal environments through hydraulic fracturing, it is essential to establish wellbore stability and understand in situ stresses. The results of the first experiments on wellbore failure in 200–450 °C granite under true triaxial stress suggest that non-catastrophic tensile and shear failure occurs in the wellbore at such temperatures, and their initiation is predictable based on existing brittle failure criterion for rocks. The results also suggest that the resultant shape of the wellbore after failure, particularly after breakout by shear failure, is not ideal for in situ stress estimation, because of the suppressed propagation of shear failure at high temperatures. In other words, there is a possibility that the high temperatures in supercritical geothermal environments contribute to wellbore stability. Therefore, extensive future studies are encouraged to examine the suppression of failure propagation at high temperatures and to clarify the underlying mechanisms.

Acknowledgments

This study was supported in part by the Japan Society for the Promotion of Science (JSPS) through Grants-in-Aid for Scientific Research (B) [Grant Number 17H03504], Challenging Research (Pioneering) [Grant Number 21K18200], and JSPS Fellows [Grant Number 20J2020108]. This study was also supported by JSPS and the Deutsche Forschungsgemeinschaft (DFG, German Research Foundation) under the Joint Research Program (JRPs-LEAD with DFG) [Grant Number JPJSJRP20181605]. K.Y. was funded by the German Federal Ministry of Education and Research (BMBF) for the GeomInt project [Grant Number 03G0866A], within the BMBF Geoscientific Research Program "Geo:N Geosciences for Sustainability." F.P. was funded by DFG, Project number PA 3451/1-1. The authors would also like to thank Toei Scientific Industrial Co., Ltd., for manufacturing the experimental system.

Data availability

The data supporting the findings of this study are available from the corresponding author upon reasonable request.

References

Batini, F., Bertini, G., Bottai, A., Burgassi, P., Cappetti, G., Gianelli, G., Puxeddu, M., 1983. San Pompeo 2 deep well: a high temperature and high pressure geothermal system, in: Strub, A., Ungemach, P. (Eds.), European Geothermal Update: Proceedings of the 3rd International Seminar on the Results of EC Geothermal Energy Research, pp. 341–353.

Baron, G., Ungemach, P., 1981. European geothermal drilling experience—problem areas and case studies, in: International Geothermal Drilling and Completions Technology Conference. Albuquerque, NM, USA, p. 24.

Brudy, M., Zoback, M.D., 1999. Drilling-induced tensile wall-fractures: implications for determination of in-situ stress orientation and magnitude. Int. J. Rock Mech. Min. Sci. 36 (2), 191–215.

Cox, S.F., 2010. The application of failure mode diagrams for exploring the roles of fluid pressure and stress states in controlling styles of fracture-controlled permeability enhancement in faults and shear zones. Geofluids 10 (1–2), 217–233.

Elders, W.A., Friðleifsson, G., Albertsson, A., 2014. Drilling into magma and the implications of the Iceland Deep Drilling project (IDDP) for high-temperature geothermal systems worldwide. Geothermics 49, 111–118.

Ewy, R.T., Cook, N.G.W., 1990. Deformation and fracture around cylindrical openings in rock—I. Obervations and analysis of deformations. Int. J. Rock. Mech. Min. Sci. & Geomech. Abstr. 27 (5), 387–407.

Espinosa-Paredes, G., Garcia-Gutierrez, A., 2003. Estimation of static formation temperatures in geothermal wells. Energy Conv. Manag. 44 (8), 1343–1355.

Fournier, R.O., 1991. The transition from hydrostatic to greater than hydrostatic fluid pressure in presently active continental hydrothermal systems in crystalline rock. Geophys. Res. Lett. 18 (5), 955–958.

Friðleifsson, G.O., Albertsson, A., Stefansson, B., Gunnlaugsson, E., Adalsteinsson, H., 2007. Deep unconventional geothermal resources: a major opportunity to harness new sources of sustainable energy, in: Proceedings, 20th World Energy Conference, Rome. World Energy Council, p. 21.

Friðleifsson, G.O., Elders, W.A., 2005. The Iceland Deep Drilling project: a search for deep unconventional geothermal resources. Geothermics 34 (3), 269–285.

Friðleifsson, G.O., Elders, W.A., Albertsson, A., 2014. The concept of the Iceland Deep Drilling project. Geothermics 49, 2–8.

Friðleifsson, G.O., Elders, W.A., 2017. The Iceland Deep Drilling project geothermal well at Reykjanes successfully reaches its supercritical target. Geotherm. Resour. Counc. Bull. 46, 30–33.

Garcia, J., Hartline, C., Walters, M., Wright, M., Rutqvist, J., Dobson, P.F., Jeanne, P., 2016. The Northwest Geysers EGS demonstration project, California: Part 1: characterization and reservoir response to injection. Geothermics 63, 97–119.

Gholami, R., Moradzadeh, A., Rasouli, V., Hanachi, J., 2014. Practical application of failure criteria in determining safe mud weight windows in drilling operations. J. Rock Mech. Geotech. Eng. 6 (1), 13–25.

Goto, R., Watanabe, N., Sakaguchi, K., Miura, T., Chen, Y., Ishibashi, T., Pramudyo, E., Pariso, F., Yoshioka, K., Nakamura, K., Komai, T., Tsuchiya, N., 2021. Creating cloud-fracture network by flow-induced microfracturing in supercritical geothermal environments. Rock Mech. Rock Eng. 54, 2959–2974.

Griffith, A.A., 1924. Theory of rupture, in: Biezeno, C.B., Burgers, J.M. (Eds.), Proceedings of the First International Congress on Applied Mechanics. J Waltman, Delft, pp. 55–63.

Hiramatsu, Y., Oka, Y., 1968. Determination of the stress in rock unaffected by boreholes or drifts, from measured strains or deformations. Int. J. Rock Mech. Min. Sci. Geomech. Abstr. 5 (4), 337–353.

Hoek, E., Brown, E.T., 1980. Underground Excavations in Rock. The Institution of Mining and Metallurgy, London.

Jaeger, J.C., Cook, N.G.W., 1979. Fundamentals of Rock Mechanics, third ed. Chapman & Hall, London.

Kato, O., Doi, N., Sakagawa, Y., Uchida, T., 1998. Fracture systematics in and around well WD-1, Kakkonda geothermal field, Japan. Geothermics 27 (5–6), 609–629.

Kinoshita, N., Abe, T., Wakabayashi, N., Ishida, T., 1997. Mechanical properties of rock at high temperatures. Doboku Gakkai Ronbunshu 1997 (561), 151–162.

Kirsch, E.G., 1898. Die Theorieder Elastizit at unddie Bedurfnisse der Festigkeitslehre, Z. Ver. Dtsch. Ing. 42 (29), 797–807.

Lee, M., Haimson, B., 1993. Laboratory study of borehole breakouts in Lac du Bonnet granite: a case of extensile failure mechanism. Int. J. Rock Mech. Min. Sci. Geomech. Abstr. 30 (7), 1039–1045.

Morita, N., Nagano, Y., 2016. Comparative analysis of various failure theories for borehole breakout predictions. SPE Annual Technical Conference and Exhibition, Dubai, UAE. OnePetro.

Moore, D.E., Lockner, D.A., Byerlee, J.D., 1994. Reduction of permeability in granite at elevated temperatures. Science 265 (5178), 1558–1561.

Morrow, C.A., Moore, D.E., Lockner, D.A., 2001. Permeability reduction in granite under hydrothermal conditions. J. Geophys. Res. Solid Earth 106 (B12), 30551–30560.

Pariseau, W.G., 2009. Design Analysis in Rock Mechanics. Taylor and Francis, London.

Parisio, F., Vinciguerra, S., Kolditz, O. and Nagel, T., 2019. The brittle-ductile transition in active volcanoes. Sci. Rep. 9 (1), 1–10.

Parisio, F., Lehmann, C., Nagel, T., 2020. A model of failure and localization of basalt at temperature and pressure conditions spanning the brittle-ductile transition. J. Geophys. Res. Solid Earth 125 (11), e2020JB020539.

Ruggieri, G., Gianelli, G., 1995. Fluid inclusion data from the Carboli 11 well, Larderello geothermal field, Italy, in: World Geothermal Congress, Italy, pp. 1087–1091.

Saishu, H., Okamoto, A., Tsuchiya, N., 2014. The significance of silica precipitation on the formation of the permeable-impermeable boundary within earth’s crust. Terra Nova 26 (4), 253–259.

Sakai, N., 1987. Mechanical behaviors of heated rocks under uniaxial compression, J. Jpn. Soc. Eng. Geol. 28 (1), 19–24.

Secor, D.T., 1965. Role of fluid pressure in jointing. Am. J. Sci. 263 (8), 633–646.

Song, I., Haimson, B.C., 1997. Polyaxial strength criteria and their use in estimating in situ stress magnitudes from borehole breakout dimensions. Int. J. Rock Mech. Min. Sci. 34 (3–4), 116.e1–116.e16.

Steingrimsson, B., Gudmundsson, A., Franzson, H., Gunnlaugsson, E., 1990. Evidence of a supercritical fluid at depth in the Nesjavellir field, in: Proceedings, 15th Workshop on Geothermal Reservoir Engineering. Stanford University, Stanford, p. 8.

Smith, R., Shaw, H., 1975. Igneous-related geothermal systems, in: White, D. Williams, D. (Eds.), Assessment of Geothermal Resources of the United States—1975. U.S. Geological Survey Circular 726, 58–83.

Smith, R., Shaw, H., 1979. Igneous-related geothermal systems, in: Muffler, L. (Ed.), Assessment of Geothermal Resources of the United States—1978. U.S. Geological Survey Circular 790, 12–17.

Tester, J.W., Anderson, B.J., Batchelor, A.S., Blackwell, D.D., DiPippo, R., Drake, E.M., Garnish, J., Livesay, B., Moore, M.C., Nichols, K., Petty, S., Toksöz, M.N., Veatch, Jr. R.W., 2006. The future of geothermal energy in the 21 century impact of enhanced geothermal systems (EGS) on the United States. MIT Press, Cambridge, MA.

Tsuchiya, N., Hirano, N., 2007. Chemical reaction diversity of geofluids revealed by hydrothermal experiments under sub- and supercritical states. Isl. Arc 16 (1), 6–15.

Tsuchiya, N., Yamada, R., Uno, M., 2016. Supercritical geothermal reservoir revealed by a granite-porphyry system. Geothermics 63, 182–194.

Tullis, J., Yund, R.A., 1977. Experimental deformation of dry Westerly granite. J. Geophys. Res. 82 (36), 5705–5718.

Violay, M., Heap, M.J., Acosta, M., Madonna, C., 2017. Porosity evolution at the brittle-ductile transition in the continental crust: implications for deep hydro-geothermal circulation. Sci. Rep. 7, 7705.

Watanabe, N., Abe, H., Okamoto, A., Nakamuraet, K., Komai, T., 2021. Formation of amorphous silica nanoparticles and its impact on permeability of fractured granite in superhot geothermal environments. Sci. Rep. 11, 5340.

Watanabe, N., Numakura, T., Sakaguchi, K., Saishu, H., Okamoto, A., Ingebritsen, S.E., Tsuchiya, N., 2017a. Potentially exploitable supercritical geothermal resources in the ductile crust. Nat. Geosci. 10 (2), 140–144.

Watanabe, N., Egawa, M., Sakaguchi, K., Ishibashi, T., Tsuchiya, N., 2017b. Hydraulic fracturing and permeability enhancement in granite from subcritical/brittle to supercritical/ductile conditions. Geophys. Res. Lett. 44 (11), 5468–5475.

Watanabe, N., Sakaguchi, K., Goto, R., Miura, T., Yamane, K., Ishibashi, T., Chen, Y., Komai, T., Tsuchiya, N., 2019. Cloud-fracture networks as a means of accessing supercritical geothermal energy. Sci. Rep. 9, 939.

Watanabe, N., Saito, K., Okamoto, A., Nakamura, K., Ishibashi, T., Saishu, H., Komai, T., Tsuchiya N., 2020. Stabilizing and enhancing permeability for sustainable and profitable energy extraction from superhot geothermal environments. Appl. Energy 260, 114306.

Weis, P., Driesner, T., Heinrich, C.A., 2012. Porphyry-copper ore shells form at stable pressure-temperature fronts within dynamic fluid plumes. Science 338 (6114), 1613–1616.

Zhao, Y., Feng, Z., Xi, B., Wan, Z., Yang, D., Liang, W., 2015. Deformation and instability failure of borehole at high temperature and high pressure in Hot Dry Rock exploitation. Renewable energy 77, 159–165.

Zoback, M.D., Moos, D., Mastin, L., Anderson, R.N., 1985. Well bore breakouts and in situ stress. J. Geophys. Res. 90 (B7), 5523–5530.